Electromagnetic Scattering from Nanosized Bodies of Revolution

with the
Green's Function Surface Integral Equation Method

Niclas Andersen

Department of Materials and Production, Physics, 2022-06

Master's Project

STUDENT REPORT
AALBORG UNIVERSITY

AALBORG UNIVERSITY
STUDENT REPORT

Department of Materials and Production
Aalborg University
Skjernvej 4a
9220 Aalborg Ø
http://www.mp.aau.dk

Title:
Electromagnetic Scattering from Nanosized Bodies of Revolution with the Green's Function Surface Integral Equation Method

Type:
Master's project

Project Period:
Spring semester 2022

Author:
Niclas Andersen

Supervisor:
Thomas Søndergaard

Page Numbers: 62

Date of Completion:
June 2, 2022

Abstract:

The problem of electromagnetic scattering from nanosized bodies of revolution is investigated with the Green's function surface integral equation method, and both the electric and magnetic field equations (EFIE) and (MFIE) are considered. The unknown equivalent surface currents are expanded in cylindrical harmonics and calculated numerically by the method of moments, with polynomial basis functions and a point matching approach.
Solutions are obtained using both quadratic and cubic basis functions, and compared with known analytic results for a sphere. It is found the cubic basis functions leads to an improvement over the quadratic, and good agreement with the analytic result is shown for a variety of dielectric parameters for both the EFIE and MFIE. For a perfect electric conducting particle, stable solutions could only be obtained from the MFIE.

Preface

This master's thesis has been written in the spring semester of 2022 at the department of materials and production, Aalborg University, as part of a master's degree in physics. The work have been supervised by Thomas Søndergaard.

Numerical calculations have been performed under a student licence of Matlab® R2022a.

References are indicated by bracketed numbers, and the full information can be found in the bibliography.

Aalborg University, June 2, 2022

Niclas Andersen

Contents

Chapter 1

Introduction

The investigating of electromagnetic scattering from nano-sized particles placed on a layered thin-film structure was the initially stated goal for the work presented. This have been considered previously in the context of improving light trapping in silicon-on-silver thin-film solar-cell configurations, e.q. for single particles or an array of particles [9], or for silver and silicon nanostrips [12]. This leads to improved light trapping in the active solar-cell layer, thus improving the absorption of light in the thin-film solar-cell. Investigating this problem with the intent to improve the coupling of light into the silicon layer was the primary motivation for considering this type of scattering problem.

The scattering problems introduced, can be modelled by Green's function integral equation methods (GFIEMs) [15][16]. Here the scattering object can be placed in free-space or on layered reference structure, like the silicon-on-silver configuration. An appropriate Green's function constructed for the reference structure can then be used to solve the integral equations for the electromagnetic fields. A surface integral approach will be used in this text, and restricting the discussion to cylindrical symmetric bodies of revolution the surface of the particle can be discretized in one dimension. A computer program have been written which solves the surface integral equations for a cylindrical symmetric scatterer in a homogeneous medium, and in order to investigate the solar-cell like structures, the Green's function should incorporate a layered reference structure, unfortunately time constraints led to this being abandoned.

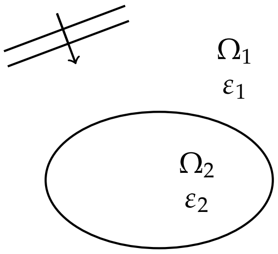

Figure 1.1: Scattering particle placed in a homogeneous medium.

Overview

In chapter 2 the theoretical foundation is presented, starting from Maxwell's equations in the frequency domain, from which the inhomogeneous wave equations can be derived. In a homogeneous medium the solutions for the electric and magnetic fields can be found with the homogeneous medium Green's function, and its closed-form expression is presented in sec. 2.2. The Green's function surface integral equations which can be derived from the wave equations is introduced in sec. 2.3, and this leads to two sets of coupled integral equations. The electric field integral equation (EFIE) and the magnetic field integral equation (MFIE), where the problem of finding the relevant field is cast in terms of the equivalent electric and magnetic surface currents.

In chapter 3 the cylindrical symmetry of the scatterer is used to reduce the dimensionality of the problem. First an appropriate surface parametrization is defined in sec. 3.1, such that the surface of the scatterer can be described as a body of revolution (BoR), with a bounding curve in two dimensions rotated around an axis of symmetry. In sec. 3.2 the problem is further reduced by expanding the unknown electric and magnetic surface currents in cylindrical harmonics, such that a single harmonic mode can be considered at a time. In secs. 3.3 and 3.4 some considerations about the incident field and boundary conditions needed to solve the integral equations are discussed.

In order to find the unknown surface currents, the EFIE and MFIE are converted to matrix equations via the method of moments in ch. 4, and the discretization scheme used is presented in sec. 4.1. Here the bounding curve is divided into sections, and on each section the surface currents are expanded in polynomial basis functions. Both quadratic and cubic functions have been used with a point matching approach. This make it possible to state the matrix equations to be solved in sec. 4.2. For a concrete numerical implementation, the matrix elements have to be calculated with an appropriate Green's function. In the case of a scatterer in a homogeneous medium, the needed Green's function can be expressed in closed form, as shown in sec. 4.3.

A program for solving the EFIE and MFIE have been developed, and some of the important choices and problems encountered are discussed in ch. 5. Accurate calculation of the matrix elements, related to the singularity of the Green's function, was the main challenge encountered, especially when using quadratic basis functions. How this was handled is discussed, before the results obtained are presented in ch. 6

Chapter 2

Theoretical Foundation

In this chapter the relevant assumptions and equations needed to investigate the problem of a scatterer in a homogeneous medium will be stated. First Maxwell's equations are stated in section 2.1, together with the wave equations for the electric and magnetic field, which must be solved with appropriate boundary conditions. The homogeneous medium Green's function, that can be used to solve these equations is introduced in section 2.2. In section 2.3 the Green's function surface integral equation method is briefly introduced and the surface integral equations for the scattering problem is stated. The well known theory presented in this chapter can be found in a variety of books on electromagnetism and relevant references will be given at the start of each section.

2.1 Maxwell's Equations in the Frequency Domain

Throughout the text it will be assumed the media under consideration are linear, local, and isotropic, furthermore only non-magnetic materials are considered. Time harmonic fields are assumed, with time dependency $e^{-i\omega t}$, which will be suppressed. Under these assumptions Maxwell's equations become [2][6][15]

$$\nabla \times \mathbf{E}(\mathbf{r}) = i\omega\mu_0 \mathbf{H}(\mathbf{r}), \tag{2.1}$$

$$\nabla \times \mathbf{H}(\mathbf{r}) = \mathbf{J}(\mathbf{r}) - i\omega\varepsilon_0\varepsilon(\mathbf{r})\mathbf{E}(\mathbf{r}), \tag{2.2}$$

$$\nabla \cdot \mathbf{D}(\mathbf{r}) = \rho(\mathbf{r}), \tag{2.3}$$

$$\nabla \cdot \mathbf{B}(\mathbf{r}) = 0, \tag{2.4}$$

where $\mathbf{E}(\mathbf{r})$ is the electric field, $\mathbf{H}(\mathbf{r})$ the magnetic field, $\mathbf{D}(\mathbf{r}) = \varepsilon_0\varepsilon(\mathbf{r})\mathbf{E}(\mathbf{r})$ the electric displacement field and $\mathbf{B}(\mathbf{r}) = \mu_0\mathbf{H}(\mathbf{r})$ is magnetic induction field. $\varepsilon(\mathbf{r})$ is the complex relative dielectric constant, $\mathbf{J}(\mathbf{r})$ the source current density and $\rho(\mathbf{r})$ is the source charge density. The frequency ω, dependency of the fields are implicit. Finally μ_0 and ε_0 are the vacuum permeability and permittivity respectively.

2.1.1 Wave Equations

The inhomogeneous wave equations for the electric and magnetic fields with a given source current density $\mathbf{J}(\mathbf{r})$, are obtained from equations 2.1 and 2.2.

$$-\nabla \times \nabla \times \mathbf{E}(\mathbf{r}) + k_0^2 \varepsilon(\mathbf{r})\mathbf{E}(\mathbf{r}) = -i\omega\mu_0 \mathbf{J}(\mathbf{r}), \tag{2.5}$$

$$-\nabla \times \frac{1}{\varepsilon(\mathbf{r})} \nabla \times \mathbf{H}(\mathbf{r}) + k_0^2 \mathbf{H}(\mathbf{r}) = -\nabla \times (\mathbf{J}(\mathbf{r})/\varepsilon(\mathbf{r})), \tag{2.6}$$

where $k_0 = \omega/c$ is the free-space wave number and $c = 1/\sqrt{\varepsilon_0\mu_0}$ is the speed of light in vacuum. These are the fundamental equations that will be considered for the scattering problem introduced. In order to solve the wave equations boundary conditions appropriate for the problem under consideration must be applied.

2.1.2 Boundary Conditions

The inhomogeneous equations are valid for any position in space and it will be assumed that $\varepsilon(\mathbf{r})$ is piecewise constant within regions Ω_i,

$$\varepsilon(\mathbf{r}) = \varepsilon_i \quad \text{for} \quad \mathbf{r} \in \Omega_i \tag{2.7}$$

A geometry with two homogeneous regions was shown in fig. 1.1, and the solution valid everywhere can be obtained by applying appropriate boundary conditions. For an interface between regions the boundary conditions for the electric and magnetic field can be obtained from Maxwell's equations or from either of the wave equations. Assuming no given surface current density they become [2]

$$\hat{\mathbf{n}} \times \mathbf{E}(\mathbf{r}_1) = \hat{\mathbf{n}} \times \mathbf{E}(\mathbf{r}_2), \tag{2.8}$$

$$\hat{\mathbf{n}} \times \mathbf{H}(\mathbf{r}_1) = \hat{\mathbf{n}} \times \mathbf{H}(\mathbf{r}_2), \tag{2.9}$$

where $\hat{\mathbf{n}}$ is the normal vector to the interface, and $\mathbf{r}_1$ and $\mathbf{r}_2$ are positions an infinitesimal distance into either Ω_1 or Ω_2. The tangential components of $\mathbf{E}$ and $\mathbf{H}$ are thus continuous across the interface, assuming non of the regions are a perfect electric conductor (PEC) [6].

For a scattering geometry like the one in fig. 1.1 a radiating boundary condition should be applied. The total field outside the scattering object must be the sum of a reference field and a scattered field propagating away from to scatterer, and the Green's function should be constructed such that it takes care of this condition [16].

2.2 Homogeneous Medium Green's Function

In this section the dyadic Green's function for a homogeneous region is introduced and rewritten in closed-form, which will be needed in the numerical implementation. Detailed derivations can be found in e.q. [2][16]. The Green's function $\mathbf{G}$, for the wave equations 2.5 and 2.6 is the solution of the same equations for a point source, and for a homogeneous region Ω_i, eq. 2.5 leads to

$$-\nabla \times \nabla \times \mathbf{G}_i(\mathbf{r}, \mathbf{r}') + k_0^2 \varepsilon_i \mathbf{G}_i(\mathbf{r}, \mathbf{r}') = -\mathbf{I}\delta(\mathbf{r} - \mathbf{r}'). \tag{2.10}$$

Here $\mathbf{I}$ is the unit dyad and $\delta(\mathbf{r} - \mathbf{r}')$ is the Dirac delta function representing a point source at $\mathbf{r}'$. Assuming the Green's function is known this leads to the solutions

$$\mathbf{E}(\mathbf{r}) = i\omega\mu_0 \int \mathbf{G}(\mathbf{r}, \mathbf{r}') \cdot \mathbf{J}(\mathbf{r}') d^3 r', \tag{2.11}$$

$$\mathbf{H}(\mathbf{r}) = \int \nabla \times \mathbf{G}(\mathbf{r}, \mathbf{r}') \cdot \mathbf{J}(\mathbf{r}') d^3 r', \tag{2.12}$$

where $\mathbf{G}(\mathbf{r}, \mathbf{r}') = \mathbf{G}_i(\mathbf{r}, \mathbf{r}')$ and it is understood that a homogeneous region Ω_i is considered. Eq. 2.12 is obtained from eqs. 2.1 and 2.11.

It can be shown that the dyadic Green's function satisfying the appropriate radiating boundary condition is

$$\mathbf{G}(\mathbf{r}, \mathbf{r}') = \left(\mathbf{I} + \frac{1}{k^2} \nabla\nabla \right) g(\mathbf{r}, \mathbf{r}'). \tag{2.13}$$

Here $\nabla\nabla$ is a dyad, $k^2 = k_0^2 \varepsilon_i$ and

$$g(\mathbf{r}, \mathbf{r}') = \frac{e^{ik|\mathbf{r}-\mathbf{r}'|}}{4\pi|\mathbf{r} - \mathbf{r}'|}, \tag{2.14}$$

is the scalar Green's function which satisfy the inhomogeneous Helmholtz equation for a point source. It is straightforward to find a closed-form expression for the homogeneous Green's function 2.13 by making the substitution $\mathbf{R} = \mathbf{r} - \mathbf{r}'$ and

$R = |\mathbf{R}|$ before differentiating. This leads to

$$\mathbf{G}(\mathbf{r}, \mathbf{r}') = \left(\mathbf{I} A(R) - \frac{\mathbf{R}}{R}\frac{\mathbf{R}}{R} B(R) \right) g(\mathbf{r}, \mathbf{r}'), \tag{2.15}$$

$$A(R) = 1 + \frac{i}{kR} - \frac{1}{(kR)^2}, \tag{2.16}$$

$$B(R) = 1 + \frac{3i}{kR} - \frac{3}{(kR)^2}. \tag{2.17}$$

It is noted how an observation point $\mathbf{r}$ in the source region leads to a singularity at $\mathbf{r} = \mathbf{r}'$, and how this can be dealt with is discussed in sec. 2.3.

For the magnetic field given by equation 2.12 the curl of the dyadic Green's function in eq. 2.13 is needed. Only the first term remains, since the curl of the gradient vanishes

$$\begin{aligned} \nabla \times \mathbf{G}(\mathbf{r}, \mathbf{r}') &= \nabla \times \left[\mathbf{I} g(\mathbf{r}, \mathbf{r}') \right], \\ &= \left[\nabla g(\mathbf{r}, \mathbf{r}') \right] \times \mathbf{I}, \end{aligned} \tag{2.18}$$

where the identity

$$\nabla \times (a\mathbf{I}) = (\nabla a) \times \mathbf{I}, \tag{2.19}$$

for a scalar function a and the unit dyadic has been used [16]. Making the same substitution for $\mathbf{r} - \mathbf{r}'$ as before, the closed-form expression for equation 2.18 is found to be

$$\nabla \times \mathbf{G}(\mathbf{r}, \mathbf{r}') = A_m(R) g(R) \frac{1}{R} \mathbf{R} \times \mathbf{I}, \tag{2.20}$$

$$A_m(R) = ik - \frac{1}{R}. \tag{2.21}$$

The curl of the Green's function is better behaved due to the vanishing $\nabla\nabla$ part of eq. 2.13.

The homogeneous Green's function presented, will be implementation in the numerical program as results obtained for a scatterer in a homogeneous medium can be compared with known analytic results, and thus serves to validate the implementation.

2.3 Green's Function Surface Integral Equation Method

The two-region three-dimensional scattering problem from 1.1, can be investigated with the Green's function surface integral equation method. Only the most impor-

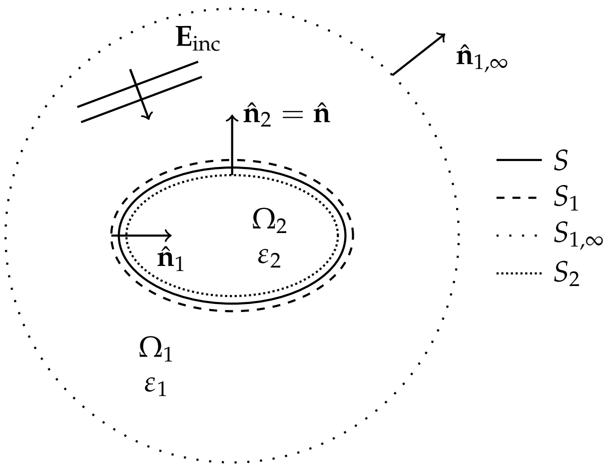

Figure 2.1: Geometry of a two-region scattering problem for which a surface integral equation can be derived. Region Ω_2 is the interior of a scattering particle of dielectric constant ε_2, placed in an otherwise homogeneous region Ω_1 with dielectric constant ε_1. The particle surface is denoted S, and S_1 and S_2 denotes surfaces placed just outside and inside S respectively. Ω_1 is bounded on the outside by a spherical surface $S_{1,\infty}$ at infinity. The surface normal vector $\hat{\mathbf{n}}_i$ points out of Ω_i. From [15]

tant assumptions and results will be stated here, and detailed derivations can be found e.q. in [3][8][13][15].

It is possible to start from either of the wave equations 2.5 or 2.6 for a homogeneous region Ω_i and the appropriate equation for the Green's function. Combining either of the wave equations with the corresponding Green's function equation and integrating over the region Ω_i, leads to a volume integral over the region, which can be converted to a surface integral by applying Gauss' theorem.

For the two region geometry considered, see fig. 2.1, Ω_1 is bounded by a spherical surface at infinity $S_{1,\infty}$ and the surface S_1 placed just outside the scatterer surface S. Ω_2 is bounded by the surface S_2 placed just inside S. The surface integral over $S_{1,\infty}$ vanishes due to the radiating boundary condition and the electric field in Ω_1 and Ω_2, is found to be [15]

$$\mathbf{E}(\mathbf{r}) = \mathbf{E}_{\text{inc}}(\mathbf{r}) + i\omega\mu_0 \oint_{S_1} \mathbf{G}_1(\mathbf{r},\mathbf{r}') \cdot \mathbf{J}_s(\mathbf{r}') d^2r' - \oint_{S_1} \nabla \times \mathbf{G}_1(\mathbf{r},\mathbf{r}') \cdot \mathbf{M}_s(\mathbf{r}') d^2r', \tag{2.22}$$

for positions $\mathbf{r} \in \Omega_1$ and

$$\mathbf{E}(\mathbf{r}) = -i\omega\mu_0 \oint_{S_2} \mathbf{G}_2(\mathbf{r},\mathbf{r}') \cdot \mathbf{J}_s(\mathbf{r}') d^2r' + \oint_{S_2} \nabla \times \mathbf{G}_2(\mathbf{r},\mathbf{r}') \cdot \mathbf{M}_s(\mathbf{r}') d^2r'. \tag{2.23}$$

for $\mathbf{r} \in \Omega_2$ where there is no incident field. The equations for the magnetic field can be obtained from the magnetic wave equation or from the electric field equations directly. The integrals involve the electric and magnetic surface current densities, defined as

$$\mathbf{J}_s(\mathbf{r}) = \hat{\mathbf{n}} \times \mathbf{H}(\mathbf{r}), \tag{2.24}$$

$$\mathbf{M}_s(\mathbf{r}) = -\hat{\mathbf{n}} \times \mathbf{E}(\mathbf{r}), \tag{2.25}$$

respectively, where $\mathbf{r}$ is a position on the scatterer surface and $\hat{\mathbf{n}}$ is the surface normal vector pointing into Ω_1. These are fictitious sources producing the same fields as the actual sources and are an example of the fundamental surface equivalence principle [1] [13]. If the equivalent surface current densities on the scatterer surface have been calculated, then the electric field in Ω_1 can be obtained from eq. 2.22.

By letting $\mathbf{r}$ approach S from either side, a set of self-consistent vector equations can be stated for the surface current densities. This leads to the electric field integral equations (EFIEs) or the magnetic field equations (MFIEs) depending on which wave equation was used as the starting point. The EFIE given next is the one presented in [15] and similar considerations lead to the MFIE.

2.3.1 Electric Field Integral Equation

$$\begin{aligned}-\mathbf{M}_s(\mathbf{r}) = \hat{\mathbf{n}} \times \mathbf{E}_{\text{inc}}(\mathbf{r}) &+ i\omega\mu_0 \oint_{S_1} \left[\hat{\mathbf{n}} \times \mathbf{G}_1(\mathbf{r},\mathbf{r}')\right] \cdot \mathbf{J}_s(\mathbf{r}') d^2r' \\ &- \oint_{S_1} \left[\hat{\mathbf{n}} \times \left(\nabla \times \mathbf{G}_1(\mathbf{r},\mathbf{r}')\right)\right] \cdot \mathbf{M}_s(\mathbf{r}') d^2r',\end{aligned} \tag{2.26a}$$

for $\mathbf{r}$ infinitesimally outside scatterer surface and

$$\begin{aligned}-\mathbf{M}_s(\mathbf{r}) = &-i\omega\mu_0 \oint_{S_2} \left[\hat{\mathbf{n}} \times \mathbf{G}_2(\mathbf{r},\mathbf{r}')\right] \cdot \mathbf{J}_s(\mathbf{r}') d^2r' \\ &+ \oint_{S_2} \left[\hat{\mathbf{n}} \times \left(\nabla \times \mathbf{G}_2(\mathbf{r},\mathbf{r}')\right)\right] \cdot \mathbf{M}_s(\mathbf{r}') d^2r',\end{aligned} \tag{2.26b}$$

for $\mathbf{r}$ infinitesimally inside scatterer surface.

2.3.2 Magnetic Field Integral Equation

$$\begin{aligned}\mathbf{J}_s(\mathbf{r}) = \hat{\mathbf{n}} \times \mathbf{H}_{\text{inc}}(\mathbf{r}) &+ i\omega\varepsilon_0\varepsilon_1 \oint_{S_1} \left[\hat{\mathbf{n}} \times \mathbf{G}_1(\mathbf{r},\mathbf{r}')\right] \cdot \mathbf{M}_s(\mathbf{r}') d^2r' \\ &+ \oint_{S_1} \left[\hat{\mathbf{n}} \times \left(\nabla \times \mathbf{G}_1(\mathbf{r},\mathbf{r}')\right)\right] \cdot \mathbf{J}_s(\mathbf{r}') d^2r',\end{aligned} \tag{2.27a}$$

for $\mathbf{r}$ infinitesimally outside scatterer surface and

$$\begin{aligned}\mathbf{J}_s(\mathbf{r}) = -i\omega\varepsilon_0\varepsilon_1 \oint_{S_2} \left[\hat{\mathbf{n}} \times \mathbf{G}_2(\mathbf{r},\mathbf{r}')\right] \cdot \mathbf{M}_s(\mathbf{r}')d^2r' \\ - \oint_{S_2} \left[\hat{\mathbf{n}} \times \left(\nabla \times \mathbf{G}_2(\mathbf{r},\mathbf{r}')\right)\right] \cdot \mathbf{J}_s(\mathbf{r}')d^2r',\end{aligned} \tag{2.27b}$$

for $\mathbf{r}$ infinitesimally inside scatterer surface. The same electric and magnetic surface currents can be determined from either the EFIEs or the MFIEs and both approaches will be considered. As mentioned in sec. 2.2, the homogeneous Green's function contains a singularity, and this leads to a needed modification of the integral equations.

2.3.3 Singularity of Green's Functions

Let $\mathcal{L}$ and $\mathcal{K}$ be defined as operators acting on $\mathbf{X}$, denoting either $\mathbf{J}_s$ or $\mathbf{M}_s$,

$$(\mathcal{L}_u\mathbf{X})(\mathbf{r}) = i\omega\mu_0 \oint_u \left[\hat{\mathbf{n}} \times \mathbf{G}_u(\mathbf{r},\mathbf{r}')\right] \cdot \mathbf{X}(\mathbf{r}')d^2r', \tag{2.28}$$

$$(\mathcal{K}_u\mathbf{X})(\mathbf{r}) = \oint_u \left[\hat{\mathbf{n}} \times \left(\nabla \times \mathbf{G}_u(\mathbf{r},\mathbf{r}')\right)\right] \cdot \mathbf{X}(\mathbf{r}')d^2r', \tag{2.29}$$

where the integral is over the surface S_u. This way the EFIE and MFIE can be stated in terms of these operators acting on the appropriate surface currents and the integrals in eqs. 2.28 and 2.29 will be denoted L- and K-type integrals, respectively.

The L-type integrals will be used in the way presented, and handled numerically by placing the observation point $\mathbf{r}$ a small distance outside the scatterer surface and utilizing an interpolation scheme to obtain the result for $\mathbf{r} \to \mathbf{r}'$ as proposed in [15].

The K-type integrals can be expressed as a principal value integral, excluding the singular point, plus a $\mathbf{X}(\mathbf{r})/2$ contribution from the singularity. This is valid if the scatterer surface is assumed to be smooth [3][15].

Dropping the s-index on the surface current densities and with the understanding that the integral in eq. 2.29 is the principle value integral, the two sets of coupled integral equations 2.26 and 2.27 can be written compactly

Coupled EFIEs

$$\hat{\mathbf{n}} \times \mathbf{E}_{\text{inc}}(\mathbf{r}) = -\frac{1}{2}\mathbf{M}(\mathbf{r}) - (\mathcal{L}_1\mathbf{J})(\mathbf{r}) + (\mathcal{K}_1\mathbf{M})(\mathbf{r}) \tag{2.30a}$$

$$0 = -\frac{1}{2}\mathbf{M}(\mathbf{r}) + (\mathcal{L}_2\mathbf{J})(\mathbf{r}) - (\mathcal{K}_2\mathbf{M})(\mathbf{r}) \tag{2.30b}$$

Coupled MFIEs

$$\hat{\mathbf{n}} \times \mathbf{H}_{\text{inc}}(\mathbf{r}) = \frac{1}{2}\mathbf{J}(\mathbf{r}) - \frac{1}{\eta_1^2}(\mathcal{L}_1\mathbf{M})(\mathbf{r}) - (\mathcal{K}_1\mathbf{J})(\mathbf{r}) \tag{2.30c}$$

$$0 = \frac{1}{2}\mathbf{J}(\mathbf{r}) + \frac{1}{\eta_2^2}(\mathcal{L}_2\mathbf{M})(\mathbf{r}) + (\mathcal{K}_2\mathbf{J})(\mathbf{r}) \tag{2.30d}$$

Here the constant $\eta_i = \sqrt{\mu_0/\varepsilon_0\varepsilon_i}$ have been introduced. After determining the equivalent electric and magnetic surface currents they can be used in eq. 2.22 or 2.23 to find the electric field at locations of interest and scattering properties can be investigated. The remainder of this text will be concerned with finding the solution to the coupled MFIEs and EFIEs for cylindrical symmetric scatterers.

Chapter 3

Bodies of Revolution

In this chapter the surface integral equations 2.30 are formulated for bodies of revolution (BoR) placed in a homogeneous medium. First an appropriate surface parametrization in two parameters is defined in sec. 3.1, together with relevant unit vectors. Then in sec. 3.2 the unknown electric and magnetic surface currents to be determined are expanding in cylindrical harmonics, such that a single harmonic mode can be considered at a time. Finally in secs. 3.3 and 3.4 some considerations about the incident field and boundary conditions needed to solve the integral equations are discussed.

A treatment of the problem can be found e.q. in the somewhat dated texts [10] or [18] or in the modern works [3] and [15]. The notation and approach in this chapter follows that of [15].

3.1 Surface Parametrization

Let the z-axis be the axis of symmetry for a body of revolution, as the one depicted in fig. 3.1a. Any point $\mathbf{s}$ on the surface of the BoR can then be parameterized by the two coordinates t and ϕ, where t denotes the distance from the starting point $\mathbf{s}_0$ along the bounding curve, see fig. 3.1b and ϕ is the azimuthal angle measured from the xz-plane.

$$\mathbf{s}(t,\phi) = \hat{\boldsymbol{\rho}} s_\rho(t) + \hat{\mathbf{z}} s_z(t), \tag{3.1}$$

where the unit vector in the ρ-direction contains the angular dependence

$$\hat{\boldsymbol{\rho}}(\phi) = \hat{\mathbf{x}} \cos\phi + \hat{\mathbf{y}} \sin\phi. \tag{3.2}$$

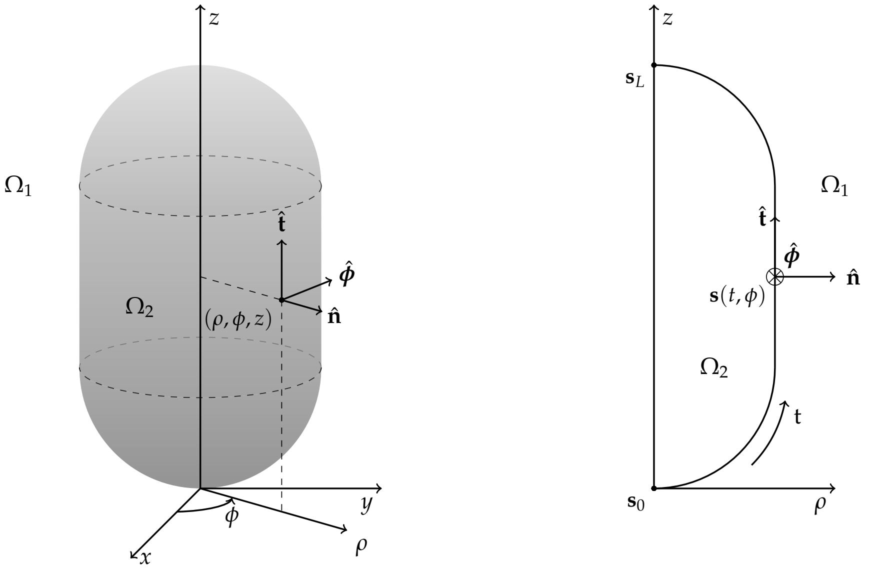

(a) **(b)**

Figure 3.1: (**a**) Scattering body of revolution in Cartesian and cylindrical coordinates with orthogonal unit vectors $(\hat{\mathbf{t}}, \hat{\boldsymbol{\phi}}, \hat{\mathbf{n}})$ defined at each surface point. (**b**) Bounding curve of length L of the BoR in the ρz-plane, parametrized by t.

The direction of increasing t is chosen to be counterclockwise, and the length of the bounding curve is denoted L, such that $\mathbf{s}_L(\phi) = \mathbf{s}(L, \phi)$ is the endpoint of the curve. The unit vectors in the t- and ϕ-direction, are defined as

$$\hat{\mathbf{t}}(t, \phi) = \frac{\partial \mathbf{s}(t, \phi)}{\partial t} \Big/ \left| \frac{\partial \mathbf{s}(t, \phi)}{\partial t} \right|, \tag{3.3}$$

$$\hat{\boldsymbol{\phi}}(\phi) = -\hat{\mathbf{x}} \sin \phi + \hat{\mathbf{y}} \cos \phi, \tag{3.4}$$

and are everywhere tangent to the surface. From these the surface normal pointing into region Ω_1 is defined as

$$\hat{\mathbf{n}}(t, \phi) = \hat{\boldsymbol{\phi}}(\phi) \times \hat{\mathbf{t}}(t, \phi), \tag{3.5}$$

so $(\hat{\mathbf{t}}, \hat{\boldsymbol{\phi}}, \hat{\mathbf{n}})$ form an orthogonal basis set, which can be used to expand the electric and magnetic surface currents. Note how the unit vectors can be expressed in terms of their $\hat{\mathbf{z}}$- and $\hat{\boldsymbol{\rho}}$-components like

$$\hat{\mathbf{t}}(t, \phi) = \hat{\boldsymbol{\rho}} t_\rho(t) + \hat{\mathbf{z}} t_z(t). \tag{3.6}$$

The example surface in fig. 3.1a, is constructed from a cylinder and two hemispherical caps at the ends to ensure the surface is smooth everywhere as assumed. Numerically the bounding curve will be constructed from straight line segments, and circle arcs preserving smoothness.

3.2 Cylindrical Harmonics Expansion

The unknown surface currents in eqs. 2.30, only have $\hat{\mathbf{t}}$- and $\hat{\boldsymbol{\phi}}$-components on the surface and due to the symmetry they can be expanded in cylindrical harmonics as [1][6]

$$\mathbf{J}(t,\phi) = \sum_{n=-\infty}^{\infty} \left(\hat{\mathbf{t}}(t,\phi) J_t^{(n)}(t) + \hat{\boldsymbol{\phi}}(\phi) J_\phi^{(n)}(t)\right) e^{in\phi}, \tag{3.7}$$

$$\mathbf{M}(t,\phi) = \sum_{n=-\infty}^{\infty} \left(\hat{\mathbf{t}}(t,\phi) M_t^{(n)}(t) + \hat{\boldsymbol{\phi}}(\phi) M_\phi^{(n)}(t)\right) e^{in\phi}, \tag{3.8}$$

where the terms like $J_t^{(n)}(t)$, are the unknowns to be determined for the nth harmonic. Similarly the incident fields in eq. 2.30 are expanded

$$\hat{\mathbf{n}}(t,\phi) \times \mathbf{E}_{\text{inc}}(t,\phi) = \sum_{n=-\infty}^{\infty} \left(-\hat{\boldsymbol{\phi}}(\phi) E_{\text{inc},t}^{(n)}(t) + \hat{\mathbf{t}}(t,\phi) E_{\text{inc},\phi}^{(n)}(t)\right) e^{in\phi}, \tag{3.9}$$

$$\hat{\mathbf{n}}(t,\phi) \times \mathbf{H}_{\text{inc}}(t,\phi) = \sum_{n=-\infty}^{\infty} \left(-\hat{\boldsymbol{\phi}}(\phi) H_{\text{inc},t}^{(n)}(t) + \hat{\mathbf{t}}(t,\phi) H_{\text{inc},\phi}^{(n)}(t)\right) e^{in\phi}. \tag{3.10}$$

Here the definition of the unit vectors in eq. 3.5 was used, and even though the fields themselves might have a normal component only the tangential components of the fields remain after the cross product with $\hat{\mathbf{n}}$.

Now the above cylindrical expansions are inserted into the integral equations 2.30. The details for the EFIEs can be found in [15] and a similar approach is used here for the MFIEs. Both sides of the equations 2.30c and 2.30d are multiplied by $e^{-im\phi}/2\pi$ and integrated over ϕ from 0 to 2π. Using the following orthogonality condition

$$\int_0^{2\pi} e^{i(n-m)\phi} d\phi = \begin{cases} 2\pi & n = m \\ 0 & n \neq m, \end{cases} \tag{3.11}$$

the left hand sides separate directly to a single harmonic when $n = m$. For the right hand sides it will be shown in sec. 4.3, that the Green's function parts, like $\hat{\mathbf{n}} \times \mathbf{G}(\mathbf{r}, \mathbf{r}')$ in eqs. 2.28 and 2.29 will be functions of $(\phi' - \phi)$. And after inserting the expansions for the surface currents, the ϕ part of the integrals will be on the form

$$\int_0^{2\pi} f(\phi' - \phi) e^{in\phi'} d\phi' = e^{in\phi} \int_0^{2\pi} f(\phi' - \phi) e^{in(\phi' - \phi)} d\phi', \tag{3.12}$$

where the integral on the right hand side is independent of the choice of ϕ. Only a single harmonic will thus remain after the multiplication with $e^{-im\phi}/2\pi$ and integrating.

The integral equations for a single harmonic n will now be stated in its t- and ϕ-components and using the differential surface element in cylindrical coordinates $d^2r' = s_\rho(t')d\phi' dt'$ they become

$$\begin{aligned}\begin{bmatrix} H^{(n)}_{\text{inc},\phi}(t) \\ -H^{(n)}_{\text{inc},t}(t) \end{bmatrix} = \frac{1}{2}\begin{bmatrix} J^{(n)}_t(t) \\ J^{(n)}_\phi(t) \end{bmatrix} &- \frac{1}{\eta_1^2}\int_{t'=0}^{L} \begin{bmatrix} L^{(n)}_{1,tt}(t,t') & L^{(n)}_{1,t\phi}(t,t') \\ L^{(n)}_{1,\phi t}(t,t') & L^{(n)}_{1,\phi\phi}(t,t') \end{bmatrix} \begin{bmatrix} M^{(n)}_t(t') \\ M^{(n)}_\phi(t') \end{bmatrix} dt' \\ &- P\int_{t'=0}^{L} \begin{bmatrix} K^{(n)}_{1,tt}(t,t') & K^{(n)}_{1,t\phi}(t,t') \\ K^{(n)}_{1,\phi t}(t,t') & K^{(n)}_{1,\phi\phi}(t,t') \end{bmatrix} \begin{bmatrix} J^{(n)}_t(t') \\ J^{(n)}_\phi(t') \end{bmatrix} dt',\end{aligned} \tag{3.13}$$

$$\begin{aligned}\begin{bmatrix} 0 \\ 0 \end{bmatrix} = \frac{1}{2}\begin{bmatrix} J^{(n)}_t(t) \\ J^{(n)}_\phi(t) \end{bmatrix} &+ \frac{1}{\eta_2^2}\int_{t'=0}^{L} \begin{bmatrix} L^{(n)}_{2,tt}(t,t') & L^{(n)}_{2,t\phi}(t,t') \\ L^{(n)}_{2,\phi t}(t,t') & L^{(n)}_{2,\phi\phi}(t,t') \end{bmatrix} \begin{bmatrix} M^{(n)}_t(t') \\ M^{(n)}_\phi(t') \end{bmatrix} dt' \\ &+ P\int_{t'=0}^{L} \begin{bmatrix} K^{(n)}_{2,tt}(t,t') & K^{(n)}_{2,t\phi}(t,t') \\ K^{(n)}_{2,\phi t}(t,t') & K^{(n)}_{2,\phi\phi}(t,t') \end{bmatrix} \begin{bmatrix} J^{(n)}_t(t') \\ J^{(n)}_\phi(t') \end{bmatrix} dt'.\end{aligned} \tag{3.14}$$

The integral kernels are defined as

$$L^{(n)}_{u,\alpha\beta}(t,t') = i\omega\mu_0 \int_{\phi'=0}^{2\pi} \hat{\alpha}(t,\phi) \cdot \left[\hat{\mathbf{n}} \times \mathbf{G}_u\left(\mathbf{s}(t,\phi), \mathbf{s}(t',\phi')\right)\right] \cdot \hat{\beta}(t',\phi') s_\rho(t') e^{in(\phi'-\phi)} d\phi', \tag{3.15}$$

$$K^{(n)}_{u,\alpha\beta}(t,t') = \int_{\phi'=0}^{2\pi} \hat{\alpha}(t,\phi) \cdot \left[\hat{\mathbf{n}} \times \left[\nabla \times \mathbf{G}_u\left(\mathbf{s}(t,\phi), \mathbf{s}(t',\phi')\right)\right]\right] \cdot \hat{\beta}(t',\phi') s_\rho(t') e^{in(\phi'-\phi)} d\phi', \tag{3.16}$$

where $\hat{\alpha}$ and $\hat{\beta}$ denotes either $\hat{\mathbf{t}}$ or $\hat{\boldsymbol{\phi}}$. Even though the surface currents are expanded in an infinite number of harmonics, the equations 3.13 and 3.14 are only solved for the significant harmonics excited by the incident field [13]. This leads to a number of solutions for $J^{(n)}_t, J^{(n)}_\phi, M^{(n)}_t$ and $M^{(n)}_\phi$ which are then used in eqs. 3.7 and 3.8 to obtain the total surface currents. Before solving the equations, the incident field and the appropriate boundary conditions will be discussed.

3.3 Incident Field

It will now be shown that for an axially incident plane wave only the $n = 1$ and $n = -1$ modes are excited, and symmetry considerations make it possible to only consider the single mode $n = 1$. [13]
An incident field propagating in the $\pm\hat{\mathbf{z}}$-direction and polarized in the $\hat{\mathbf{x}}$-direction is chosen

$$\mathbf{E}_0(\mathbf{r}) = \hat{\mathbf{x}} E_0 e^{\pm i k_1 z}, \tag{3.17}$$

where the $+$ or $-$ gives a plane wave respectively from below and above. From eq. 2.1 the corresponding incident magnetic field is

$$\mathbf{H}_0(\mathbf{r}) = \frac{1}{i\omega\mu_0} \nabla \times \mathbf{E}_0(\mathbf{r}) = \pm \frac{1}{\eta_1} E_0 e^{\pm i k_1 z} \hat{\mathbf{y}} \tag{3.18}$$

where the definitions $k_i = k_0\sqrt{\varepsilon_i}$ and $\eta_i = \sqrt{\mu_0/\varepsilon_0\varepsilon_i}$ from earlier have been used.

The t- and ϕ-components of the nth harmonic for the known incident fields in eqs. 3.9 and 3.10 can now be obtained from [15]

$$H_{0,\alpha}^{(n)}(t) = \frac{1}{2\pi} \int_{\phi=0}^{2\pi} \mathbf{H}_0(\mathbf{r}) \cdot \hat{\alpha} e^{-in\phi} d\phi, \tag{3.19}$$

and similarly for the electric field. Using the expressions for $\hat{\boldsymbol{\rho}}$, $\hat{\boldsymbol{\phi}}$ and $\hat{\mathbf{t}}$ in eqs. 3.2, 3.4 and 3.6, the integral over ϕ can be carried out e.q.

$$\begin{aligned} H_{0,t}^{(n)}(t) &= \frac{1}{2\pi} \int_{\phi=0}^{2\pi} \mathbf{H}_0(\mathbf{r}) \cdot \hat{\mathbf{t}} e^{-in\phi} d\phi = \pm \frac{t_\rho(t)}{2\pi\eta_1} E_0 e^{\pm i k_1 z} \int_{\phi=0}^{2\pi} \sin(\phi) e^{-in\phi} d\phi \\ &= \pm \frac{t_\rho(t)}{2\eta_1} E_0 e^{\pm i k_1 z} \begin{cases} -i & n = 1 \\ i & n = -1, \end{cases} \end{aligned} \tag{3.20}$$

As the orthogonality of the trigonometric functions ensures the integral is zero for any other n. Similarly the other components can be found.

$$H_{0,\phi}^{(n)}(t) = \pm \frac{1}{2\eta_1} E_0 e^{\pm i k_1 z} \begin{cases} 1 & n = 1 \\ 1 & n = -1, \end{cases} \tag{3.21}$$

$$E_{0,t}^{(n)}(t) = \frac{t_\rho(t)}{2} E_0 e^{\pm i k_1 z} \begin{cases} 1 & n = 1 \\ 1 & n = -1, \end{cases} \tag{3.22}$$

$$E_{0,\phi}^{(n)}(t) = \frac{1}{2} E_0 e^{\pm i k_1 z} \begin{cases} i & n = 1 \\ -i & n = -1. \end{cases} \tag{3.23}$$

Inserting back in the expansion for the H-field in eq. 3.10 and dropping the arguments of the unit vectors one obtains

$$\begin{aligned}\hat{\mathbf{n}}(t,\phi)\times\mathbf{H}_{\text{inc}}(t,\phi) &= \pm\frac{1}{2\eta_1}E_0e^{\pm ik_1z}\left[\left(\hat{\mathbf{t}}+t_\rho i\hat{\boldsymbol{\phi}}\right)e^{i\phi}+\left(\hat{\mathbf{t}}-t_\rho i\hat{\boldsymbol{\phi}}\right)e^{-i\phi}\right]\\ &= \pm\frac{1}{\eta_1}E_0e^{\pm ik_1z}\left[\hat{\mathbf{t}}\cos\phi-\hat{\boldsymbol{\phi}}t_\rho\sin\phi\right].\end{aligned} \tag{3.24}$$

A similar argument can be made for the electric field. This makes it clear that it is possible to only consider the single harmonic n when an axially incident plane wave is chosen as the excitation and from now on the index for the harmonic will be suppressed.

3.4 Boundary Conditions

Before solving eqs. 3.13 and 3.14, the boundary conditions for the problem have to be considered. In the following an open bounding curve, like the one for the scatterer in fig. 3.1 is assumed, and special care must be taken for the two endpoints $\mathbf{s}_0$ and $\mathbf{s}_L$ on the z-axis. Here the currents must be independent of ϕ and for the $n=1$ harmonic the current expansion in eq. 3.7 becomes

$$\mathbf{J}(0,\phi)=\left[\hat{\mathbf{t}}(0,\phi)J_t(0)+\hat{\boldsymbol{\phi}}(\phi)J_\phi(0)\right]e^{i\phi} \tag{3.25}$$

for the startpoint. Furthermore $\hat{\mathbf{t}}$ must be equal to $\hat{\boldsymbol{\rho}}$ to ensure the surface is smooth across the z-axis. For the angles $\phi=0$ and $\phi=\pi/2$ specifically, one obtains

$$\mathbf{J}(0,0)=\hat{\mathbf{x}}J_t(0)+\hat{\mathbf{y}}J_\phi(0), \tag{3.26}$$

$$\mathbf{J}(0,\pi/2)=\hat{\mathbf{y}}iJ_t(0)-\hat{\mathbf{x}}iJ_\phi(0). \tag{3.27}$$

Equating these, the boundary condition for the surface current at the start point is

$$J_\phi(0)=iJ_t(0). \tag{3.28}$$

Similar considerations for the endpoint, where $\hat{\mathbf{t}}=-\hat{\boldsymbol{\rho}}$ leads to

$$J_\phi(L)=-iJ_t(L). \tag{3.29}$$

The same boundary conditions apply for the magnetic surface current in 3.8.

Additionally the derivative of the surface currents across the symmetry axis must vanish in order to avoid that the current results in a field singularity.

Chapter 4

Solution by the Method of Moments for a BoR

In this chapter the method of moments, outlined in appendix A, is used to find the unknown surface currents on a body of revolution excited by an axially incident plane wave. The magnetic field integral equations 3.13 and 3.14, developed using the cylindrical symmetry will be considered. In sec. 4.1 the discretization scheme which allows an expansion of the surface currents in quadratic or cubic basis functions, will be presented. This leads to the formulation of a matrix equation in sec. 4.2 suitable for numerical implementation. For the problem of homogeneous scatterer in a homogeneous background medium, the matrix elements needed will be calculated in sec. 4.3. The approach in this chapter follows that of [15], where the EFIE have been considered.

4.1 Discretization

In chapter 3 it was shown how the cylindrical symmetry of a body of revolution makes it possible to parametrized the surface in the t and ϕ coordinates as shown in fig. 3.1. In order to calculate the surface currents, the bounding curve is now divided into N_k sections, as illustrated in one dimension in fig. 4.1. Each section k is further divided into two subsections and the start, interior and end points are denoted $t_k^{(0)}$, $t_k^{(1)}$, $t_k^{(2)}$ respectively. For each section k the surface currents $J_\alpha(t)$ and $M_\alpha(t)$, from eqs. 3.7 and 3.8, are expanded in a number of basis functions. Similar

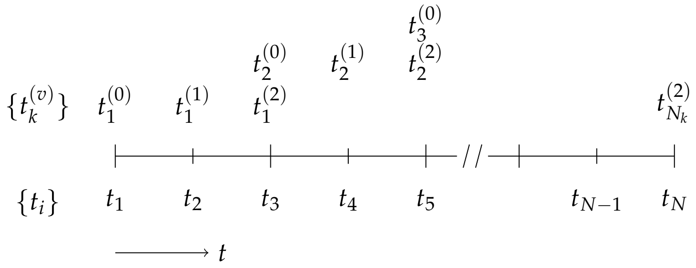

Figure 4.1: Discretization of the bounding curve for a BoR parametrized by t. The curve is divided into N_k sections where the start, interior and end points for section k is given by $t_k^{(0)}$, $t_k^{(1)}$ and $t_k^{(2)}$ respectively. $\{t_i\}$ denotes the N unique sample points along the bounding curve.

to eq. A.2, this leads to the following expansion along the bounding curve

$$J_\alpha(t) = \sum_{k=1}^{N_k} \sum_{v} f_k^{(v)}(t) J_{\alpha,k}^{(v)}, \tag{4.1}$$

$$M_\alpha(t) = \sum_{k=1}^{N_k} \sum_{v} f_k^{(v)}(t) M_{\alpha,k}^{(v)}, \tag{4.2}$$

Here $f_k^{(v)}(t)$ are the basis functions for section k to be defined, and the unknown local coefficients for section k are $J_{\alpha,k}^{(v)}$ and $M_{\alpha,k}^{(v)}$, for $\alpha = t$ or ϕ.

Let i denote the unique sample points $\{t_i\}$ along the curve, see fig. 4.1, such that each point is only counted once, and let N be the number of those sample points. By a point matching approach, where the testing functions are defined as Dirac delta functions $\delta_i(t - t_i)$, the surface current and incident field at specific sample points i can be organized in vectors

$$\overline{J}_\alpha = \begin{bmatrix} J_{\alpha,1} & J_{\alpha,2} & \dots & J_{\alpha,N} \end{bmatrix}^T, \tag{4.3}$$

$$\overline{M}_\alpha = \begin{bmatrix} M_{\alpha,1} & M_{\alpha,2} & \dots & J_{\alpha,N} \end{bmatrix}^T, \tag{4.4}$$

$$\overline{H}_{\text{inc},\alpha} = \begin{bmatrix} H_{\text{inc},\alpha,1} & H_{\text{inc},\alpha,2} & \dots & H_{\text{inc},\alpha,N} \end{bmatrix}^T. \tag{4.5}$$

These global coefficients must be related to the local coefficients defined within each section. The approach differs for the quadratic and cubic polynomials, that will be used as basis function, and will be shown separately.

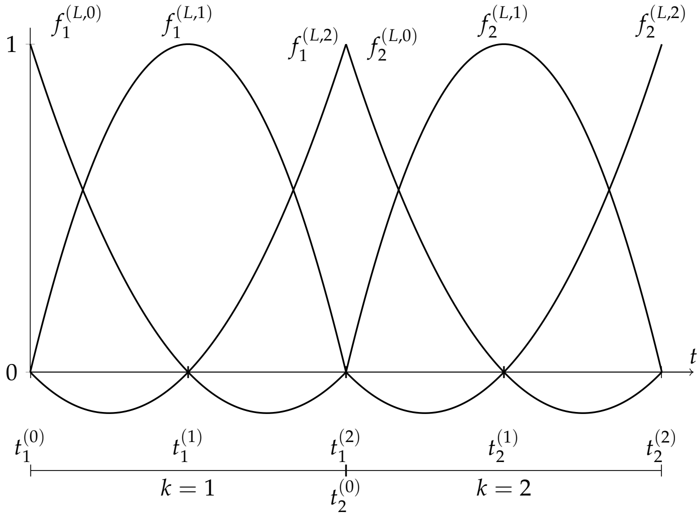

Figure 4.2: Quadratic basis functions for the two first sections.

4.1.1 Point Matching Quadratic Polynomials

The quadratic Lagrange interpolation polynomials, see sec. A.2.1, appropriate for a section with start and end points $t_k^{(0)}$ and $t_k^{(2)}$ are

$$f_k^{(L,v)}(t) = f^{(L,v)}\left(\frac{t - t_k^{(0)}}{|t_k^{(2)} - t_k^{(0)}|}\right), \quad v = 0, 1, 2 \tag{4.6}$$

where $f^{(L,v)}$ are the quadratic polynomials defined on the unit interval in eqs. A.11. In fig. 4.2 they are shown for the first two sections. Note how continuity between the sections are ensured by the functions $f_1^{(L,2)}$ and $f_2^{(L,0)}$.

The quadratic polynomials sample at the start, middle and end point of a section, and to relate the local coefficients in eqs. 4.1 and 4.2 to the global coefficients in eqs. 4.3 and eqs. 4.4 the local coefficients are expressed as vectors

$$\overline{J}_{\alpha,k} = \begin{bmatrix} J_{\alpha,k}^{(0)} & J_{\alpha,k}^{(1)} & J_{\alpha,k}^{(2)} \end{bmatrix}^T, \tag{4.7}$$

$$\overline{M}_{\alpha,k} = \begin{bmatrix} M_{\alpha,k}^{(0)} & M_{\alpha,k}^{(1)} & M_{\alpha,k}^{(2)} \end{bmatrix}^T, \tag{4.8}$$

and a relation matrix $\overline{\overline{P}}_k$ between these and the global coefficients can be defined as

$$\begin{array}{cc} & \begin{array}{ccccccc} 1 & \dots & 2k-1 & 2k & 2k+1 & \dots & N \end{array} \\ \overline{\overline{P}}_k = & \begin{bmatrix} 0 & \dots & 1 & 0 & 0 & \dots & 0 \\ 0 & \dots & 0 & 1 & 0 & \dots & 0 \\ 0 & \dots & 0 & 0 & 1 & \dots & 0 \end{bmatrix}. \end{array} \tag{4.9}$$

This way the relations can be expressed as

$$\overline{J}_{\alpha,k} = \overline{\overline{P}}_k \overline{J}_\alpha, \tag{4.10}$$

$$\overline{M}_{\alpha,k} = \overline{\overline{P}}_k \overline{M}_\alpha. \tag{4.11}$$

The relations for the cubic polynomials are presented next.

4.1.2 Point matching Cubic Polynomials

The cubic Hermite spline polynomials $f^{(H,v)}$ are defined on the unit interval in eqs. A.12 in appendix A. The unit interval is sampled at both end points, and continuity of the first derivative across section boundaries is ensured. The cubic polynomials suitable for a point matching approach are now developed from those on the unit interval.

Let the index k run over all N global sample points, such that t_1 is the first sample point, and t_N the last. Instead of sampling at the endpoints of a section, the polynomials $f^{(H,1)}$ and $f^{(H,0)}$, from eqs. A.12 are defined on the subsections of k, $[t_k^{(0)}, t_k^{(1)}]$ and $[t_k^{(1)}, t_k^{(2)}]$ respectively, and similarly for $f^{(H,3)}$ and $f^{(H,2)}$. This leads to the two piecewise combined polynomials $f_k^{(CH,0)}$ and $f_k^{(CH,1)}$, defined on $[t_k^{(0)}, t_k^{(2)}]$, shown for the first three sections in fig. 4.3. Note how adjacent sections overlap and how the first section only have a single subsection from $t_1 = t_2^{(0)}$ to

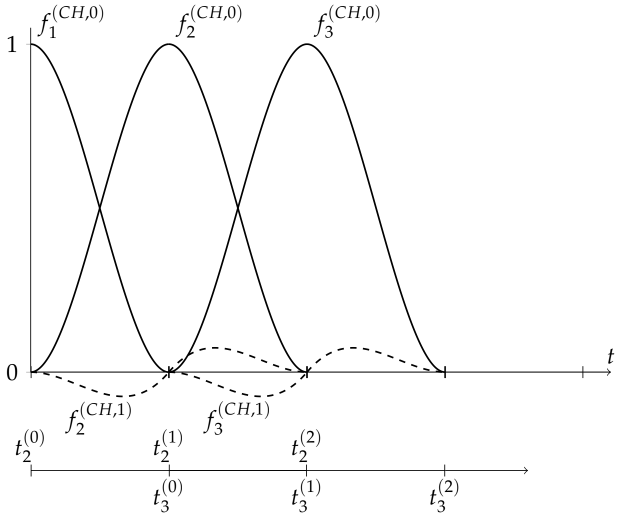

Figure 4.3: Piecewise combined cubic polynomials for the first three sections. $f_k^{(CH,0)}$ ensures continuity and $f_k^{(CH,1)}$ ensures a continuous first derivative.

$t_2 = t_2^{(1)}$. The last section is handled similarly.

$$f_k^{(CH,0)}(t) = \begin{cases} f^{(H,1)}\left(\frac{t-t_k^{(0)}}{|t_k^{(1)}-t_k^{(0)}|}\right), & t_k^{(0)} \leq t < t_k^{(1)}, \quad 1 < k < N \\ f^{(H,0)}\left(\frac{t-t_k^{(1)}}{|t_k^{(2)}-t_k^{(1)}|}\right), & t_k^{(1)} \leq t \leq t_k^{(2)}, \quad 1 < k < N \\ f^{(H,0)}\left(\frac{t}{|t_2|}\right), & 0 \leq t < t_2, \quad k = 1 \\ f^{(H,1)}\left(\frac{t-t_{N-1}}{|t_N-t_{N-1}|}\right), & t_{N-1} \leq t \leq t_N, \quad k = N \end{cases} \tag{4.12a}$$

$$f_k^{(CH,1)}(t) = \begin{cases} |t_k^{(1)} - t_k^{(0)}| f^{(H,3)}\left(\frac{t-t_k^{(0)}}{|t_k^{(1)}-t_k^{(0)}|}\right), & t_k^{(0)} \leq t < t_k^{(1)}, \quad 1 < k < N \\ |t_k^{(2)} - t_k^{(1)}| f^{(H,2)}\left(\frac{t-t_k^{(1)}}{|t_k^{(2)}-t_k^{(1)}|}\right), & t_k^{(1)} \leq t \leq t_k^{(2)}, \quad 1 < k < N \\ |t_2| f^{(H,3)}\left(\frac{t}{|t_2|}\right), & 0 \leq t < t_2, \quad k = 1 \\ |t_N - t_{N-1}| f^{(H,2)}\left(\frac{t-t_{N-1}}{|t_N-t_{N-1}|}\right), & t_{N-1} \leq t \leq t_N, \quad k = N \end{cases} \tag{4.12b}$$

The combined polynomials sample at the interior point of a section, where $f_k^{(CH,0)}$ ensures continuity and $f_k^{(CH,1)}$ ensures continuity of the first derivative. For the first and last sample point, $f_k^{(CH,1)}$ is defined to make sure the derivative vanishes at those points. This way the boundary conditions for the derivative at the z-axis, discussed in sec. 3.4 are taken care of. For $f_k^{(CH,1)}$ the length of each subsection is multiplied on $f^{(H,2)}$ or $f^{(H,3)}$ to ensure a derivative of one.

Similarly to how a relation matrix $\overline{\overline{P}}_k$, was defined for the quadratic basis polynomials in the previous section. One must be constructed for the cubic basis polynomials in order to relate the local and global coefficients. For the cubic basis functions the expansion of the electric surface current along the bounding curve, eq. 4.1, becomes

$$J_\alpha(t) = \sum_{k=1}^{N} f_k^{(CH,0)}(t) J_{\alpha,k}^{(0)} + f_k^{(CH,1)}(t) J_{\alpha,k}^{(1)}. \tag{4.13}$$

Since $f_k^{(CH,0)}$ samples at every point, $J_{\alpha,k}^{(0)}$ corresponds to the current at the global sample point i, $J_{\alpha,i=k}$, defined in eq. 4.3. $J_{\alpha,k}^{(1)}$ representing the derivative of the current at $t_k = t_k^{(1)}$ must also be related to the global sample points. In order to do this, an expression for the derivative at a global sample point must be developed.

Consider a second order Taylor expansion of the current about the point t_i

$$J_\alpha(t) \approx A + B(t - t_i) + C(t - t_i)^2, \tag{4.14}$$

where A, B and C are the usual Taylor coefficients. B is then the first order derivative at $t_{k=i}$, such that $B = J_{\alpha,k}^{(1)}$. This can be expressed in terms of the global current at adjacent points t_{i-1} and t_{i+1} by considering the system of equations

$$J_{\alpha,i} = J_\alpha(t_i) = A, \tag{4.15}$$

$$J_{\alpha,i-1} = A + B(t_{i-1} - t_i) + C(t_{i-1} - t_i)^2, \tag{4.16}$$

$$J_{\alpha,i+1} = A + B(t_{i+1} - t_i) + C(t_{i+1} - t_i)^2. \tag{4.17}$$

Inserting $J_{\alpha,i}$ into the last two equations, the matrix equation becomes

$$\begin{bmatrix} (t_{i-1} - t_i) & (t_{i-1} - t_i)^2 \\ (t_{i+1} - t_i) & (t_{i+1} - t_i)^2 \end{bmatrix} \begin{bmatrix} B \\ C \end{bmatrix} = \begin{bmatrix} J_{\alpha,i-1} - J_{\alpha,i} \\ J_{\alpha,i+1} - J_{\alpha,i} \end{bmatrix}. \tag{4.18}$$

Let $\overline{\overline{D}}$ denote the matrix to the left, then by matrix inversion the solution for B is found

$$B = b_0 J_{\alpha,i-1} + b_1 J_{\alpha,i} + b_2 J_{\alpha,i+1}, \tag{4.19}$$

$$b_0 = \frac{1}{\det \overline{\overline{D}}}(t_{i+1} - t_i)^2, \tag{4.20}$$

$$b_1 = \frac{1}{\det \overline{\overline{D}}}[(t_{i-1} - t_i)^2 - (t_{i+1} - t_i)^2], \tag{4.21}$$

$$b_2 = \frac{-1}{\det \overline{\overline{D}}}(t_{i-1} - t_i)^2. \tag{4.22}$$

The relation matrix for the combined cubic polynomials can now be constructed as

$$\overline{\overline{P}}_k = \begin{array}{c} \begin{array}{ccccccc} 1 & \dots & k-1 & k & k+1 & \dots & N \end{array} \\ \begin{bmatrix} 0 & \dots & 0 & 1 & 0 & \dots & 0 \\ 0 & \dots & b_0 & b_1 & b_2 & \dots & 0 \end{bmatrix} \end{array}, \quad 1 < k < N. \tag{4.23}$$

For $k = 1$ or $k = N$, the second row is all zeros as the derivative must vanish at the z-axis. The relation between the local coefficients from eq. 4.13

$$\overline{J}_{\alpha,k} = \begin{bmatrix} J_{\alpha,k}^{(0)} & J_{\alpha,k}^{(1)} \end{bmatrix}^T, \tag{4.24}$$

and the global coefficients from eq. 4.3 can finally be expressed as

$$\overline{J}_{\alpha,k} = \overline{\overline{P}}_k \overline{J}_{\alpha}. \tag{4.25}$$

The relation is the same for the magnetic currents.

4.2 Matrix Equations

The MFIEs 3.13 and 3.14 will now be formulated as a combined matrix equation. The first step is inserting the expansions 4.1 and 4.2 into eq. 3.13 and testing with $\delta_i(t - t_i)$ as was done for the currents in eq. 4.3. For a specific i this leads to

$$\begin{aligned} \begin{bmatrix} H_{\mathrm{inc},\phi,i} \\ -H_{\mathrm{inc},t,i} \end{bmatrix} = \frac{1}{2}\begin{bmatrix} J_{t,i} \\ J_{\phi,i} \end{bmatrix} - \frac{1}{\eta_1^2}\sum_{k=1}^{N_k}\sum_{v}\int_{t'=0}^{L} \begin{bmatrix} L_{1,tt}(t_i,t') & L_{1,t\phi}(t_i,t') \\ L_{1,\phi t}(t_i,t') & L_{1,\phi\phi}(t_i,t') \end{bmatrix} \begin{bmatrix} f_k^{(v)}(t')M_{t,k}^{(v)} \\ f_k^{(v)}(t')M_{\phi,k}^{(v)} \end{bmatrix} dt' \\ - \sum_{k=1}^{N_k}\sum_{v}\int_{t'=0}^{L} \begin{bmatrix} K_{1,tt}(t_i,t') & K_{1,t\phi}(t_i,t') \\ K_{1,\phi t}(t_i,t') & K_{1,\phi\phi}(t_i,t') \end{bmatrix} \begin{bmatrix} f_k^{(v)}(t')J_{t,k}^{(v)} \\ f_k^{(v)}(t')J_{\phi,k}^{(v)} \end{bmatrix} dt'. \end{aligned} \tag{4.26}$$

Here the vectors with the local current coefficients like eq. 4.7 can be used to rewrite as

$$\begin{aligned}\begin{bmatrix} H_{\text{inc},\phi,i} \\ -H_{\text{inc},t,i} \end{bmatrix} = \frac{1}{2}\begin{bmatrix} J_{t,i} \\ J_{\phi,i} \end{bmatrix} - \frac{1}{\eta_1^2}\sum_{k=1}^{N_k}\begin{bmatrix} \overline{L}_{1,tt,i,k} & \overline{L}_{1,t\phi,i,k} \\ \overline{L}_{1,\phi t,i,k} & \overline{L}_{1,\phi\phi,i,k} \end{bmatrix}\begin{bmatrix} \overline{M}_{t,k} \\ \overline{M}_{\phi,k} \end{bmatrix} \\ - \sum_{k=1}^{N_k}\begin{bmatrix} \overline{K}_{1,tt,i,k} & \overline{K}_{1,t\phi,i,k} \\ \overline{K}_{1,\phi t,i,k} & \overline{K}_{1,\phi\phi,i,k} \end{bmatrix}\begin{bmatrix} \overline{J}_{t,k} \\ \overline{J}_{\phi,k} \end{bmatrix},\end{aligned} \tag{4.27}$$

where $\overline{L}$ and $\overline{K}$ are row vectors with three or two elements for quadratic and cubic basis functions respectively. The elements are given as

$$\left[\overline{L}_{u,\alpha\beta,i,k}\right]_v = \int_{t'=t_k^{(0)}}^{t_k^{(2)}} L_{u,\alpha\beta}(t_i,t') f_k^{(v)}(t')dt', \tag{4.28a}$$

$$\left[\overline{K}_{u,\alpha\beta,i,k}\right]_v = \int_{t'=t_k^{(0)}}^{t_k^{(2)}} K_{u,\alpha\beta}(t_i,t') f_k^{(v)}(t')dt', \tag{4.28b}$$

where $f_k^{(v)}(t')$ are the functions from eq. 4.6 or 4.12. In the same way as equation 4.27 was derived, eq. 3.14 can be formulated as a matrix equation.

By using the relations between local and global coefficients from either eq. 4.10 or 4.25 depending on the chosen basis functions the matrix systems for the coupled MFIEs and EFIEs from eq. 2.30, can finally be stated.

Coupled MFIE

$$\begin{bmatrix} \overline{H}_{\text{inc},\phi} \\ -\overline{H}_{\text{inc},t} \\ \overline{0} \\ \overline{0} \end{bmatrix} = \begin{bmatrix} \left(-\overline{\overline{K}}_{1,tt} + \frac{1}{2}\overline{\overline{I}}\right) & -\overline{\overline{K}}_{1,t\phi} & -\frac{1}{\eta^2}\overline{\overline{L}}_{1,tt} & -\frac{1}{\eta^2}\overline{\overline{L}}_{1,t\phi} \\ -\overline{\overline{K}}_{1,\phi t} & \left(-\overline{\overline{K}}_{1,\phi\phi} + \frac{1}{2}\overline{\overline{I}}\right) & -\frac{1}{\eta^2}\overline{\overline{L}}_{1,\phi t} & -\frac{1}{\eta^2}\overline{\overline{L}}_{1,\phi\phi} \\ \left(\overline{\overline{K}}_{2,tt} + \frac{1}{2}\overline{\overline{I}}\right) & \overline{\overline{K}}_{2,t\phi} & \frac{1}{\eta^2}\overline{\overline{L}}_{2,tt} & \frac{1}{\eta^2}\overline{\overline{L}}_{2,t\phi} \\ \overline{\overline{K}}_{2,\phi t} & \left(\overline{\overline{K}}_{2,\phi\phi} + \frac{1}{2}\overline{\overline{I}}\right) & \frac{1}{\eta^2}\overline{\overline{L}}_{2,\phi t} & \frac{1}{\eta^2}\overline{\overline{L}}_{2,\phi\phi} \end{bmatrix} \begin{bmatrix} \overline{J}_t \\ \overline{J}_\phi \\ \overline{M}_t \\ \overline{M}_\phi \end{bmatrix} \tag{4.29a}$$

Coupled EFIE

$$\begin{bmatrix} \overline{E}_{\text{inc},\phi} \\ -\overline{E}_{\text{inc},t} \\ \overline{0} \\ \overline{0} \end{bmatrix} = \begin{bmatrix} -\overline{\overline{L}}_{1,tt} & -\overline{\overline{L}}_{1,t\phi} & \left(\overline{\overline{K}}_{1,tt} - \frac{1}{2}\overline{\overline{I}}\right) & \overline{\overline{K}}_{1,t\phi} \\ -\overline{\overline{L}}_{1,\phi t} & -\overline{\overline{L}}_{1,\phi\phi} & \overline{\overline{K}}_{1,\phi t} & \left(\overline{\overline{K}}_{1,\phi\phi} - \frac{1}{2}\overline{\overline{I}}\right) \\ \overline{\overline{L}}_{2,tt} & \overline{\overline{L}}_{2,t\phi} & \left(-\overline{\overline{K}}_{2,tt} - \frac{1}{2}\overline{\overline{I}}\right) & -\overline{\overline{K}}_{2,t\phi} \\ \overline{\overline{L}}_{2,\phi t} & \overline{\overline{L}}_{2,\phi\phi} & -\overline{\overline{K}}_{2,\phi t} & \left(-\overline{\overline{K}}_{2,\phi\phi} - \frac{1}{2}\overline{\overline{I}}\right) \end{bmatrix} \begin{bmatrix} \overline{J}_t \\ \overline{J}_\phi \\ \overline{M}_t \\ \overline{M}_\phi \end{bmatrix} \tag{4.29b}$$

In the coupled matrix equations, the $N \times N$ submatrices are defined as

$$\overline{\overline{L}}_{u,\alpha\beta} = \sum_{i=1}^{N} \sum_{k=1}^{N_k} \overline{P}_i \overline{L}_{u,\alpha\beta,i,k} \overline{\overline{P}}_k \tag{4.30}$$

$$\overline{\overline{K}}_{u,\alpha\beta} = \sum_{i=1}^{N} \sum_{k=1}^{N_k} \overline{P}_i \overline{K}_{u,\alpha\beta,i,k} \overline{\overline{P}}_k \tag{4.31}$$

where $\overline{P}_i$ is a column vector of zeros, except for a one at index i.

For a numerical implementation the elements given in eq. 4.28 needs to be calculated. This means inserting eqs. 3.15 and 3.16 and performing the double integration in t' and ϕ'.

$$\left[\overline{L}_{u,\alpha\beta,i,k}\right]_v =$$

$$i\omega\mu_0 \int_{t'=t_k^{(0)}}^{t_k^{(2)}} \int_{\phi'=0}^{2\pi} \hat{\alpha}(t,\phi) \cdot \left[\hat{\mathbf{n}} \times \mathbf{G}_u\big(\mathbf{s}(t,\phi), \mathbf{s}(t',\phi')\big)\right] \cdot \hat{\beta}(t',\phi') f_k^{(v)}(t') s_\rho(t') e^{i(\phi'-\phi)} d\phi' dt' \tag{4.32a}$$

$$\left[\overline{K}_{u,\alpha\beta,i,k}\right]_v =$$

$$\int_{t'=t_k^{(0)}}^{t_k^{(2)}} \int_{\phi'=0}^{2\pi} \hat{\alpha}(t,\phi) \cdot \left[\hat{\mathbf{n}} \times \left[\nabla \times \mathbf{G}_u\big(\mathbf{s}(t,\phi), \mathbf{s}(t',\phi')\big)\right]\right] \cdot \hat{\beta}(t',\phi') f_k^{(v)}(t') s_\rho(t') e^{i(\phi'-\phi)} d\phi' dt' \tag{4.32b}$$

where $t = t_i$ and $\phi = \phi_i$ such that $\mathbf{s}(t,\phi)$ is the sample point i. In the next section it will be shown how the integration kernels can be expressed explicitly for a scatterer in a homogeneous medium.

The theory presented leading to the coupled EFIE and MFIE in eq. 4.29 is valid for both PEC and dielectric scatterers, but for a PEC scatterer the electric field vanishes inside the surface, and the equations reduce to

MFIE (PEC)

$$\begin{bmatrix} \overline{H}_{\text{inc},\phi} \\ -\overline{H}_{\text{inc},t} \end{bmatrix} = \begin{bmatrix} \left(-\overline{\overline{K}}_{1,tt} + \frac{1}{2}\overline{\overline{I}}\right) & -\overline{\overline{K}}_{1,t\phi} \\ -\overline{\overline{K}}_{1,\phi t} & \left(-\overline{\overline{K}}_{1,\phi\phi} + \frac{1}{2}\overline{\overline{I}}\right) \end{bmatrix} \begin{bmatrix} \overline{J}_t \\ \overline{J}_\phi \end{bmatrix} \tag{4.33a}$$

EFIE (PEC)

$$\begin{bmatrix} \overline{E}_{\text{inc},\phi} \\ -\overline{E}_{\text{inc},t} \end{bmatrix} = \begin{bmatrix} -\overline{\overline{L}}_{1,tt} & -\overline{\overline{L}}_{1,t\phi} \\ -\overline{\overline{L}}_{1,\phi t} & -\overline{\overline{L}}_{1,\phi\phi} \end{bmatrix} \begin{bmatrix} \overline{J}_t \\ \overline{J}_\phi \end{bmatrix} \tag{4.33b}$$

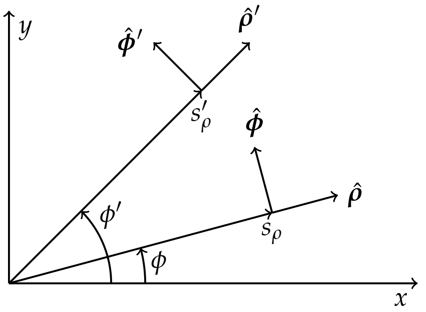

Figure 4.4: ρ and ϕ unit vectors for an observation point $\mathbf{s}$ and a source point $\mathbf{s}'$ in the xy plane.

4.3 Matrix Elements for Homogeneous Medium Green's Function

The Green's function parts in eqs. 4.32 will now be considered for a scatterer in a homogeneous medium. The Green's function enters in the integral kernels as

$$\hat{\alpha}(t,\phi)\cdot\left[\hat{\mathbf{n}}\times\mathbf{G}\left(\mathbf{s}(t,\phi),\mathbf{s}(t',\phi')\right)\right]\cdot\hat{\beta}(t',\phi'), \tag{4.34}$$

for the L matrix elements, and

$$\hat{\alpha}(t,\phi)\cdot\left[\hat{\mathbf{n}}\times\left[\nabla\times\mathbf{G}\left(\mathbf{s}(t,\phi),\mathbf{s}(t',\phi')\right)\right]\right]\cdot\hat{\beta}(t',\phi'), \tag{4.35}$$

for the K matrix elements. These terms are now found explicitly for the homogeneous Green's function in eq. 2.15.

The relevant unit vectors from section 3.1 needed for $\hat{\alpha}$ and $\hat{\beta}' = \hat{\beta}(t',\phi')$ are stated below in terms of the $(\hat{\boldsymbol{\rho}},\hat{\boldsymbol{\phi}},\hat{\mathbf{z}})$ unit vectors, see fig. 4.4. The arguments (t,ϕ) and (t',ϕ') have been dropped to ease notation.

$$\begin{aligned}
\hat{\boldsymbol{\rho}} &= \hat{\mathbf{x}}\cos\phi+\hat{\mathbf{y}}\sin\phi & \hat{\boldsymbol{\rho}}' &= \hat{\boldsymbol{\rho}}\cos(\phi'-\phi)+\hat{\boldsymbol{\phi}}\sin(\phi'-\phi)\\
\hat{\boldsymbol{\phi}} &= -\hat{\mathbf{x}}\sin\phi+\hat{\mathbf{y}}\cos\phi & \hat{\boldsymbol{\phi}}' &= -\hat{\boldsymbol{\rho}}\sin(\phi'-\phi)+\hat{\boldsymbol{\phi}}\cos(\phi'-\phi)\\
\hat{\mathbf{t}} &= \hat{\boldsymbol{\rho}}t_\rho+\hat{\mathbf{z}}t_z & \hat{\mathbf{t}}' &= \hat{\boldsymbol{\rho}}'t'_\rho+\hat{\mathbf{z}}t'_z\\
\hat{\mathbf{n}} &= \hat{\boldsymbol{\rho}}n_\rho+\hat{\mathbf{z}}n_z & \hat{\mathbf{n}}' &= \hat{\boldsymbol{\rho}}'n'_\rho+\hat{\mathbf{z}}n'_z\\
\mathbf{s} &= \hat{\boldsymbol{\rho}}s_\rho+\hat{\mathbf{z}}s_z & \mathbf{s}' &= \hat{\boldsymbol{\rho}}'s'_\rho+\hat{\mathbf{z}}s'_z
\end{aligned} \tag{4.36}$$

The vector $\mathbf{R}$ from a source point to an observation point, both on the surface, can now be given in cylindrical coordinates as

$$\mathbf{R} = \mathbf{s} - \mathbf{s}' = \hat{\boldsymbol{\rho}}(s_\rho - s'_\rho \cos(\phi' - \phi)) - \hat{\boldsymbol{\phi}} s'_\rho \sin(\phi' - \phi) + \hat{\mathbf{z}}(s_z - s'_z), \tag{4.37}$$

and the length of $\mathbf{R}$ is

$$R = |\mathbf{R}| = \sqrt{(s_\rho - s'_\rho)^2 + 2 s_\rho s'_\rho (1 - \cos(\phi' - \phi)) + (s_z - s'_z)^2}. \tag{4.38}$$

4.3.1 L Matrix Elements

Ignoring the scalars for now in eq. 2.15, the anterior vector product in eq. 4.34 gives rise to two dyadic terms $\hat{\alpha} \cdot [\hat{\mathbf{n}} \times \mathbf{I}] \cdot \hat{\beta}'$ and $\hat{\alpha} \cdot [\hat{\mathbf{n}} \times \mathbf{RR}] \cdot \hat{\beta}'$.

For the unit dyadic term, the dyadic identity $\mathbf{a} \cdot (\mathbf{b} \times \mathbf{C}) = (\mathbf{a} \times \mathbf{b}) \cdot \mathbf{C}$ [17] is used to get

$$\hat{\alpha} \cdot (\hat{\mathbf{n}} \times \mathbf{I}) \cdot \hat{\beta}' = (\hat{\alpha} \times \hat{\mathbf{n}}) \cdot \mathbf{I} \cdot \hat{\beta}' = (\hat{\alpha} \times \hat{\mathbf{n}}) \cdot \hat{\beta}', \tag{4.39}$$

where the cross product is easily handled by remembering the definition 3.5. For the four different combinations of unit vectors this leads to

$$\begin{aligned}
\hat{\mathbf{t}} \cdot (\hat{\mathbf{n}} \times \mathbf{I}) \cdot \hat{\mathbf{t}}' &= (\hat{\mathbf{t}} \times \hat{\mathbf{n}}) \cdot \hat{\mathbf{t}}' = \hat{\boldsymbol{\phi}} \cdot \hat{\mathbf{t}}' = t'_\rho \sin(\phi' - \phi) \\
&= -n'_z \sin(\phi' - \phi), && (4.40a)\\
\hat{\mathbf{t}} \cdot (\hat{\mathbf{n}} \times \mathbf{I}) \cdot \hat{\boldsymbol{\phi}}' &= \cos(\phi' - \phi), && (4.40b)\\
\hat{\boldsymbol{\phi}} \cdot (\hat{\mathbf{n}} \times \mathbf{I}) \cdot \hat{\mathbf{t}}' &= -(n_z n'_z \cos(\phi' - \phi) + n_\rho n'_\rho), && (4.40c)\\
\hat{\boldsymbol{\phi}} \cdot (\hat{\mathbf{n}} \times \mathbf{I}) \cdot \hat{\boldsymbol{\phi}}' &= -n_z \sin(\phi' - \phi). && (4.40d)
\end{aligned}$$

The relationship between the components of the tangential and normal vectors $t_\rho = -n_z$ and $t_z = n_\rho$ have been used to simplify the expressions.

To find the explicit expressions for the $\hat{\alpha} \cdot [\hat{\mathbf{n}} \times \mathbf{RR}] \cdot \hat{\beta}'$ term, the vector product between $\hat{\mathbf{n}}$ and $\mathbf{R}$ has to be calculated. Both have been expressed in the same cylindrical unit vectors so the vector product is readily found

$$\begin{aligned}
\hat{\mathbf{n}} \times \mathbf{R} = {} & \hat{\boldsymbol{\rho}}[n_z s'_\rho \sin(\phi' - \phi)] + \hat{\boldsymbol{\phi}}[n_z(s_\rho - s'_\rho \cos(\phi' - \phi)) - n_\rho(s_z - s'_z)] \\
& + \hat{\mathbf{z}}[-n_\rho s'_\rho \sin(\phi' - \phi)]. && (4.41)
\end{aligned}$$

Now $(\hat{\mathbf{n}} \times \mathbf{R})\mathbf{R}$ is a dyadic and the final result is obtained by taking the scalar products from the left and right with the appropriate unit vectors from eqs. 4.36.

A bit of algebra leads to

$$
\begin{aligned}
\hat{\mathbf{t}}\cdot(\hat{\mathbf{n}}\times\mathbf{R})\mathbf{R}\cdot\hat{\mathbf{t}}' &= -s'_\rho \sin{(\phi'-\phi)}[n'_\rho(s_z-s'_z) - n'_z(s_\rho\cos{(\phi'-\phi)}-s'_\rho)], \qquad &(4.42\text{a})\\
\hat{\mathbf{t}}\cdot(\hat{\mathbf{n}}\times\mathbf{R})\mathbf{R}\cdot\hat{\boldsymbol{\phi}}' &= s_\rho s'_\rho \sin^2(\phi'-\phi), &(4.42\text{b})\\
\hat{\boldsymbol{\phi}}\cdot(\hat{\mathbf{n}}\times\mathbf{R})\mathbf{R}\cdot\hat{\mathbf{t}}' &= [n_z(s_\rho - s'_\rho\cos(\phi'-\phi)) - n_\rho(s_z-s'_z)]\\
&\quad\cdot[n'_\rho(s_z-s'_z) - n'_z(s_\rho\cos(\phi'-\phi)-s'_\rho)], &(4.42\text{c})\\
\hat{\boldsymbol{\phi}}\cdot(\hat{\mathbf{n}}\times\mathbf{R})\mathbf{R}\cdot\hat{\boldsymbol{\phi}}' &= -s_\rho\sin(\phi'-\phi)[n_z(s_\rho - s'_\rho\cos(\phi'-\phi)) - n_\rho(s_z-s'_z)]. &(4.42\text{d})
\end{aligned}
$$

Remembering the scalar terms from eqs. 2.14, 2.16 and 2.17, the expression for the Green's function used for the L matrix elements becomes

$$
\hat{\alpha}\cdot\big[\hat{\mathbf{n}}\times\mathbf{G}(\mathbf{s},\mathbf{s}')\big]\cdot\hat{\beta}' = \big[(\hat{\alpha}\cdot[\hat{\mathbf{n}}\times\mathbf{I}]\cdot\hat{\beta}')A(R) - \frac{1}{R^2}(\hat{\alpha}\cdot[\hat{\mathbf{n}}\times\mathbf{RR}]\cdot\hat{\beta}')B(R)\big]g(R), \tag{4.43}
$$

for the different combinations of $\hat{\alpha}$ and $\hat{\beta}'$ in eq. 4.40 and eq. 4.42.

4.3.2 K Matrix Elements

The curl of the homogeneous Green's function from eq. 2.20 is inserted in the expression 4.35, and again ignoring the scalar terms and suppressing the arguments one obtains

$$
\begin{aligned}
\hat{\alpha}\cdot(\hat{\mathbf{n}}\times[\nabla\times\mathbf{G}(\mathbf{s},\mathbf{s}')])\cdot\hat{\beta}' &\propto \hat{\alpha}\cdot(\hat{\mathbf{n}}\times[\mathbf{R}\times\mathbf{I}])\cdot\hat{\beta}'\\
&= \hat{\alpha}\cdot[\mathbf{R}(\hat{\mathbf{n}}\cdot\mathbf{I}) - (\hat{\mathbf{n}}\cdot\mathbf{R})\mathbf{I}]\cdot\hat{\beta}'\\
&= \hat{\alpha}\cdot\mathbf{R}\hat{\mathbf{n}}\cdot\hat{\beta}' - \hat{\alpha}\cdot(\hat{\mathbf{n}}\cdot\mathbf{R})\hat{\beta}',
\end{aligned} \tag{4.44}
$$

where the dyadic identity [17]

$$
\mathbf{a}\times(\mathbf{b}\times\mathbf{C}) = \mathbf{b}(\mathbf{a}\cdot\mathbf{C}) - (\mathbf{a}\cdot\mathbf{b})\mathbf{C}, \tag{4.45}
$$

was used to rewrite the double cross term. To find the explicit matrix elements, the different combinations of $\hat{\alpha}\cdot\mathbf{R}$, $\hat{\mathbf{n}}\cdot\hat{\beta}'$, $\hat{\mathbf{n}}\cdot\mathbf{R}$, and $\hat{\alpha}\cdot\hat{\beta}'$ must be evaluated. For the first term in eq. 4.44 the scalar products are

$$
\begin{aligned}
\hat{\mathbf{t}}\cdot\mathbf{R} &= -n_z(s_\rho - s'_\rho\cos(\phi'-\phi)) + n_\rho(s_z-s'_z), \qquad &(4.46\text{a})\\
\hat{\boldsymbol{\phi}}\cdot\mathbf{R} &= -s_\rho\sin(\phi'-\phi), &(4.46\text{b})\\
\hat{\mathbf{n}}\cdot\hat{\mathbf{t}}' &= -n_\rho n'_z\cos(\phi'-\phi) + n_z n'_\rho, &(4.46\text{c})\\
\hat{\mathbf{n}}\cdot\hat{\boldsymbol{\phi}}' &= -n_\rho\sin(\phi'-\phi). &(4.46\text{d})
\end{aligned}
$$

For the second term the needed scalar products are

$$\begin{aligned}
\hat{\mathbf{t}} \cdot \hat{\mathbf{t}}' &= n_z n_z' \cos(\phi' - \phi) + n_\rho n_\rho', && \text{(4.47a)} \\
\hat{\mathbf{t}} \cdot \hat{\boldsymbol{\phi}}' &= n_z \sin(\phi' - \phi), && \text{(4.47b)} \\
\hat{\boldsymbol{\phi}} \cdot \hat{\mathbf{t}}' &= -n_z' \sin(\phi' - \phi), && \text{(4.47c)} \\
\hat{\boldsymbol{\phi}} \cdot \hat{\boldsymbol{\phi}}' &= \cos(\phi' - \phi), && \text{(4.47d)} \\
\hat{\mathbf{n}} \cdot \mathbf{R} &= n_\rho (s_\rho - s_\rho' \cos(\phi' - \phi)) + n_z (s_z - s_z'). && \text{(4.47e)}
\end{aligned}$$

Reintroducing the scalars from eq. 2.20, the Green's function used for the K matrix elements becomes

$$\hat{\alpha} \cdot (\hat{\mathbf{n}} \times [\nabla \times \mathbf{G}(\mathbf{s}, \mathbf{s}')]) \cdot \hat{\beta}' = (\hat{\alpha} \cdot \mathbf{R}\hat{\mathbf{n}} \cdot \hat{\beta}' - \hat{\alpha} \cdot (\hat{\mathbf{n}} \cdot \mathbf{R}) \hat{\beta}') A_m(R) \frac{g(R)}{R}, \tag{4.48}$$

for the different combinations of $\hat{\alpha}$ and $\hat{\beta}'$ in eqs. 4.46 and 4.47.

All that is needed to solve the EFIE or MFIE for a BoR scatterer in a homogeneous medium have thus been presented. The rest of the text is concerned with the numerical implementation and results.

Chapter 5

Numerical Implementation

In this chapter the implementation of the program developed for solving the EFIE and MFIE for cylindrical symmetric scatterers is discussed. In the case of a dielectric scatterer the equations were given in eqs. 4.29 and for a PEC scatterer in eqs. 4.33. In order to verify the program the canonical example of plane wave scattering by a homogeneous sphere is explored, see fig. 5.1a. Here analytic solutions for the surface currents can be found for both dielectric or perfect conducting spheres, see appendix B, and it will thus serve as a basis for assessing the accuracy of solutions for the EFIE and MFIE.

After a short overview of the parts of the program, some choices made and problems encountered are discussed. Results obtained are presented in the next chapter.

5.1 Overview of Program

The developed program for solving the EFIE and MFIE consist of several steps and is summarized below, with references to relevant sections.

- Problem definition, ch. 1.
- Discretization of bounding curve, sec. 4.1.
- Calculation of incident fields, sec. 3.3.
- Calculation of matrix elements, sec. 4.3.
- Setup the matrix equation sec. 4.2, using the boundary conditions, sec 3.4.

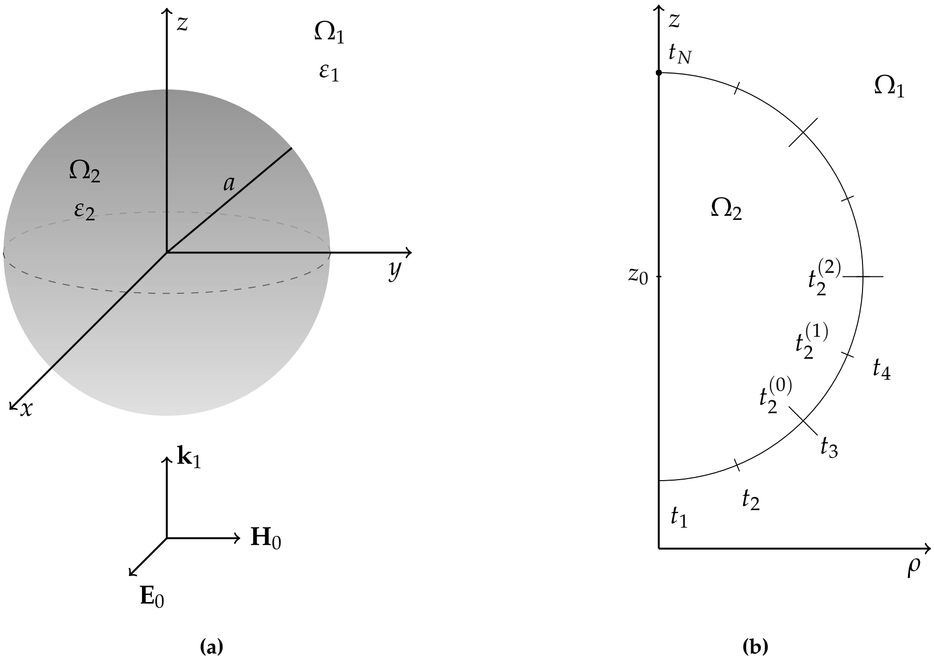

Figure 5.1: (**a**) PEC or dielectric sphere of radius a and dielectric constant ε_2 placed in a homogeneous background medium of dielectric constant ε_1. Illuminated from below by a plane wave polarized in the $\hat{\mathbf{x}}$-direction. (**b**) Discretization scheme for the sphere considered. The first three observation/sample points t_i, $i = 1, 2, 3$ are shown together with the three points $t_2^{(v)}$, $v = 0, 1, 2$ associated with the second section.

- Calculate surface currents by solving the matrix equation.
- Use calculated surface currents to calculate properties of interest.

5.1.1 Problem Definition

The program handles both PEC and dielectric cylindrical symmetric scatterers. The first step is to decide which type to consider and whether to use the EFIE or MFIE formulation, such that one of the four matrix equations in 4.29 and 4.33 is used. In order to solve the relevant equation one must choose the quadratic or cubic basis functions for the expansion of the surface currents, and the number of sections N_k for the expansions.

The dielectric constants of the scatterer ε_2 and background medium ε_1, and the wavelength λ of the incident plane wave, must be defined. Finally the parameters defining the geometry of the problem must be given, for a sphere this means the radius a and z-coordinate of the center z_0.

5.1.2 Discretization

Following the approach presented in sec. 4.1, the bounding curve of length L for the scatterer is divided into N_k sections, each with one interior point, see fig. 5.1b. For an open bounding curve, this lead to the total number of discrete sample points $N = 2N_k + 1$, where the two endpoints, $t_i = t_1 = 0$ and $t_i = t_N = L$, denotes the t-parameter at those points. The bounding curve for $\phi = 0$ is used, such that the ρz-plane coincides with the xz-plane.

For the computation of the matrix elements, components of the surface positions $\mathbf{s}(t_i, 0)$, $\mathbf{s}(t', \phi')$ and normal vectors $\hat{\mathbf{n}}(t_i, 0)$, $\hat{\mathbf{n}}(t', \phi')$ are needed. In order to integrate in the source coordinates, they need to be properly parametrized along the surface. For a sphere this means every section have the same curvature and the normal vector points out of the sphere in the direction from the center to the source point. In principle any bounding curve could be used, provided it is smooth and parametrized properly in t, see e.q. fig. 3.1, where straight and curved sections are combined.

5.1.3 Incident Fields

The t and ϕ components of the relevant incident field must be calculated for all N-sample points, according to eqs. 3.20-3.23. The incident plane wave can be from below or above.

5.1.4 Calculation of Matrix Elements

In the matrix equations 4.29 or 4.33, the elements of the submatrices, like $\overline{\overline{L}}_{1,tt}$ or $\overline{\overline{K}}_{1,tt}$, must be calculated according to eqs. 4.32. Accurate numerical evaluation of the integrals have been the primary challenge in the implementation of the program, and some thoughts about the chosen approach are now presented.

For the matrix elements where the sample point i is outside section k the integrals are straightforwardly calculated with the 'integral2' routine in Matlab®, which numerically evaluates double integrals, to some specified degree of accuracy. When a sample point is located at either the endpoints $t_k^{(0)}$ or $t_k^{(2)}$, or interior point $t_k^{(1)}$ of a section, the singular nature of the homogeneous-medium Green's function must be addressed. Such a section will be referred to as a self-section.

K-type Elements

For the K-type integrals it was discussed in sec. 2.3.3, how the integral must be evaluated as a principal value integral. To this a contribution like $\frac{1}{2}\mathbf{J}_s$, is added, and this current term enters in the matrix equations as $\overline{\overline{I}}/2$. Since the singular points are known, the principal value integrals in 4.32b, can be performed for self-sections by excluding a small part of the integration domain around the singular point. It was found this leads to convergent integrals.

L-type Elements

As mentioned in sec. 2.3.3, the evaluation of the L-type integrals, in eq. 4.32a, is handled for self-sections by placing the sample position a very small distance δ outside the surface, see fig. 5.2a, where the case of a sample point at the end of a section is shown. In practice the distance from source point to observation point R in eq. 4.38 is made non zero by moving the observation point a small distance in the direction of the unit vector

$$\mathbf{s} = \mathbf{s}_\delta = \hat{\boldsymbol{\rho}}(s_\rho + \delta n_\rho) + \mathbf{z}(s_z + \delta n_z). \tag{5.1}$$

This allows integration along the curve for a self-section without R becoming zero. The integral is evaluated for a few δ-values and the value of a specific matrix element $L_{ik}^{(v)}$ is extrapolated to $\delta = 0$, using either a third order polynomial fit or a logarithmic fit, given by

$$L_{ik}^{(v)}(\delta) = c_0 + c_1\delta + c_2\delta^2 + c_3\delta^3 \quad \text{or} \tag{5.2}$$

$$L_{ik}^{(v)}(\delta) = c_0 + c_1 \log \delta, \tag{5.3}$$

where the highest coefficient of determination determines which to use. An example of a sample point at the end of a section, where a logarithmic fit was necessary is shown in fig. 5.2b. The constant value c_0 from the best fit is taken as the value of the integral at $\delta = 0$, where it would otherwise be singular. The real and imaginary parts are fitted separately as one might be singular and the other not.

For the 'integral2' routine it is possible to integrate singularities on the boundary of regions of integration if they are not too severe [14]. To make sure the singularities are on the boundary, the limits on t' is split at $t_k^{(1)}$. As illustrated in fig. 5.2b, some of the matrix elements have singularities which are severe enough, that the integral does not converge when δ is close to zero. This was especially pronounced when using the quadratic basis functions.

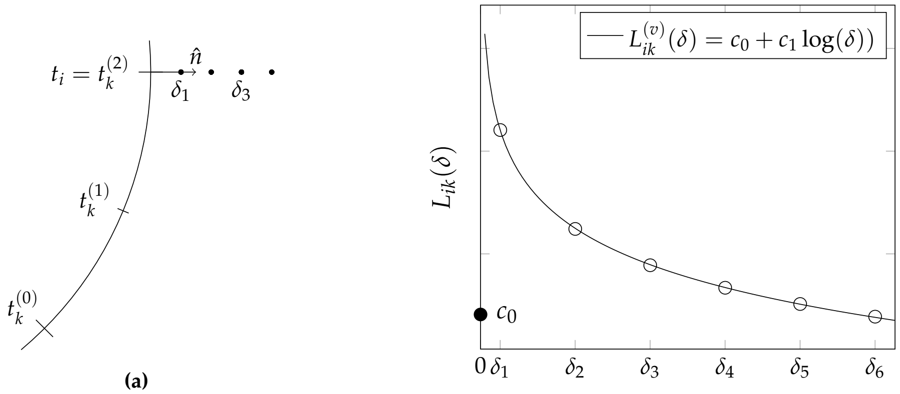

(a)

(b)

Figure 5.2: Illustrating the interpolation scheme to handle the singularity when integrating over a self-section. (**a**) The sample point t_i is pushed a small distance δ away from the bounding curve in the direction of $\hat{\mathbf{n}}$ and the integration is performed for a number of δ's. (**b**) Example of the integral results obtained for six different delta values. The curve is the best logarithmic fit, and the constant c_0 the value obtained for the given matrix element.

5.1.5 Matrix Equation and Boundary Conditions

After the evaluation of the the matrix elements, the boundary conditions from sec. 3.4 must be applied. Taking the EFIE for a PEC from eq. 4.33b, as an example. Then condition 3.28, $J_\phi(0) = iJ_t(0)$, for the start point on the axis, can be applied by first setting the $(N+1)$'th row in the matrix to zero and then inserting i as the first element in the same row, and -1 at position $(N+1)$. Finally the $(N+1)$'th element in the vector with the incident field components is set to zero, which leads to the condition

$$0 = -iJ_{t,1} + J_{\phi,1}, \tag{5.4}$$

forcing the appropriate boundary condition for the start point, similarly can be done for the end point.

The boundary condition that the derivative must vanish at the end points, are automatically taken care of for the cubic basis functions as mentioned in sec. 4.1.2. But is not guaranteed for the quadratic basis functions, this will be discussed further in the next chapter.

5.1.6 Calculated Surface Currents

The matrix equation is solved by inversion, and the vectors of coefficients for the surface currents, at the N discrete sample points is obtained. For a PEC, this means the vectors $\overline{J}_t$, $\overline{J}_\phi$, and additionally $\overline{M}_t$, $\overline{M}_\phi$ for a dielectric scatterer. Inserting these together with the chosen basis functions in the appropriate expansions of $J_\alpha(t)$ and $M_\alpha(t)$ in sec. 4.1, the surface currents can be calculated everywhere along the bounding curve.

5.1.7 Properties of Interest

In order to verify the program, a sphere was initially chosen as the scattering object, as analytic results are available, see. appendix B. The results presented in the next chapter will mainly be concerned with assessing the accuracy of the implementation and as a way to quantify this, the following expression for the integrated error have been used

$$\Sigma = \Sigma_t + \Sigma_\phi, \tag{5.5}$$

and for each of the components $\alpha = t$ or ϕ the integrated error have been defined as

$$\Sigma_\alpha = \int_0^1 \frac{\left|J_\alpha(t) - J_\alpha^{Mie}(t)\right|^2}{\left|J_\alpha^{Mie}(t)\right|^2} dt, \tag{5.6}$$

where $J_\alpha(t)$ is the α-component of the calculated electric surface current , and $J_\alpha^{Mie}(t)$ is the analytic Mie-scattering result. The integrated error for the magnetic surface current have been calculated the same way. Note that t have been normalized.

For a scattering problem some of the main properties of interest are the scattering, absorption and extinction cross sections [15]. After the surface currents have been calculated they can be used to determine the cross sections, but due to time constraints only the implementation of the absorption cross section calculation was implemented, and the expression used is stated here for reference. For a cylindrical symmetric scatterer, the power absorbed is given by [15]

$$P_{\text{abs}} = -2\pi \sum_n \int_t \frac{1}{2} \text{Real}\left[\left(J_\phi^{(n)}(t)\right)^* M_t^{(n)}(t) - \left(J_t^{(n)}(t)\right)^* M_\phi^{(n)}(t)\right] s_\rho(t) dt, \tag{5.7}$$

where the $*$ denotes complex conjugation. This can be calculated directly from the expressions for the surface currents along the bounding curve. In the case of a incident plane wave, the absorption cross section can be obtained from the power absorbed as

$$\sigma_{\text{abs}} = \frac{P_{\text{abs}}}{\frac{1}{2} n_1 |\mathbf{E}_{\text{inc}}|^2 \sqrt{\varepsilon_0/\mu_0}}. \tag{5.8}$$

Chapter 6

Results and Discussion

The results presented in this chapter will mainly be concerned with the validation of the numerical implementation. This will also serve as a comparison of the performance of the EFIE and MFIE formulations, when using either the quadratic or cubic basis functions.

The scattering problem considered is that of a sphere in free-space, illuminated from below by a $\hat{\mathbf{x}}$-polarized plane wave with some wavelength λ, see fig. 5.1a. Spheres of different radii will be considered and their radius will be given in terms of the wavelength. The parameter t have been normalized with the length of the bounding curve t_N, such that $t/t_N = 0$ denotes the bottom point of the sphere, and $t/t_N = 1$ the top point of the sphere. The electric surface current have been normalized with the amplitude of the incident magnetic field, and the magnetic surface current with the amplitude of the electric field.

First results obtained using the EFIE for a PEC sphere will be considered in sec. 6.1. These will serve to present some of the difficulties encountered, as they were especially pronounced in this case. Then the MFIE is used to investigate the same PEC sphere in sec. 6.2 and a comparison between the two formulations will be made. Next, results for dielectric spheres for both the EFIE and MFIE is presented in sec. 6.3, including the special cases of high dielectric constant and lossy spheres. Finally in sec. 6.4, the absorption cross section of a spherical gold particle will be used as a final validation of the implementation.

6.1 EFIE for a PEC Sphere

6.1.1 Varying δ for Self-Sections

For the evaluation of the L-type matrix elements for self-sections, small δ-values have to be chosen, as mentioned in sec. 5.1.4. A way to quantify an appropriately small minimum δ value for a given geometry is thus sought.

In order to illustrate this problem the EFIE 4.33b, for a perfect electric conducting sphere of radius $\lambda/2$ in free-space, was used. Both the quadratic f^L, and the cubic basis functions f^{CH} were employed on the bounding curve discretized in $N_k = 10$ sections of equal length L_k. The smallest delta value δ_1, was chosen as a percentage of L_k. Six delta values evenly spaced between δ_1 and $\delta_{\text{max}} = 5\delta_1$ were used, and the program was run ten times with δ_1/L_k being varied from 0.25‰ to 1%. For the smallest δ_1, the results are shown in fig. 6.1, where the normalized absolute value of the components of the surface current are plotted together with the analytic Mie-solution. There is some deviation, especially near the top and bottom of the sphere, and this will be explored further in the next subsection.

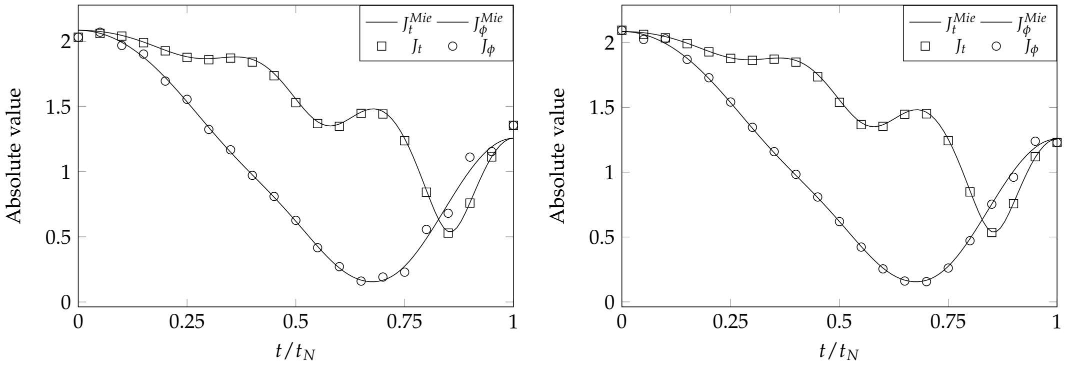

(a) Quadratic basis functions **(b)** Cubic basis functions

Figure 6.1: Normalized absolute value of t- and ϕ-components of the electric surface current along the bounding curve of a PEC sphere with radius $\lambda/2$. Obtained using the EFIE with 21 sample points and six evenly spaced deltas such that, $\delta_1/L_k = 0.25‰$ and $\delta_{\text{max}}/L_k = 1.25‰$. For both (**a**) quadratic and (**b**) cubic basis functions there is decent agreement with the analytic expression, but some deviation near the endpoints is observed.

For each of the ten runs the integrated error from eq. 5.5 was calculated and the results are shown in fig. 6.2a. For the quadratic basis functions it is clear, that

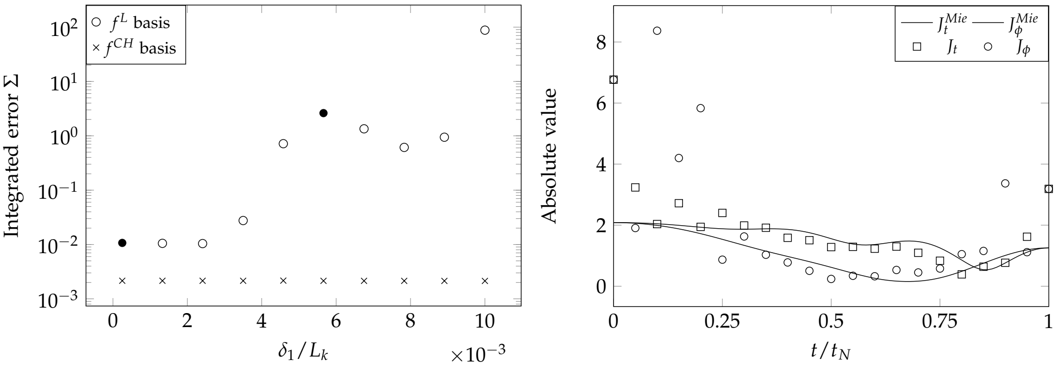

(a)

(b) f^L and $\delta_1/L_k = 5.66$‰ used.

Figure 6.2: (**a**) Integrated error for varying δ_1/L_k, for the problem considered in fig. 6.1. The error when using the quadratic basis functions f^L, depends strongly on the chosen δ_1. The first solid marker shows the error for $\delta_1/L_k = 0.25$‰, see. fig. 6.1a, and the second solid marker for $\delta_1/L_k = 5.66$‰, where the absolute values of the surface current is shown in (**b**). Both the t- and ϕ-components deviates strongly from analytic result.

the choice of delta greatly influences the results. In general, increasing δ_1 leads to larger integrated error, but there are certain intervals where increasing the distance between sample point and bounding curve leads to smaller errors. In this case from around 5.5‰ to 8‰, leading to a local top in the integrated error marked by the second filled dot. This have been consistent with what was found for other geometries and delta values. For the local top at $\delta_1/L_k = 5.66$‰ the integrated error was found to be more than 200 times that of $\delta_1/L_k = 0.25$‰ and the surface currents obtained when using $\delta_1/L_k = 5.66$‰ are shown in fig. 6.2b. Here large deviations especially near the top and bottom are seen, this is discussed in the next section. The results obtained with the cubic basis functions was significantly less sensitive to changes in δ_i and for the specific example, the errors for all δ_i-values deviated less than one percent.

The results in this section was obtained from a specific geometry and choice of delta values, but similar results have been obtained for a range of parameters. It has not been possible to find a condition for determining δ-values leading to stable results, especially for the quadratic basis functions, even when increasing the number of sample points.

6.1.2 Quadratic or Cubic Basis Functions

Additional insight into the problems encountered near the axis of symmetry can be gained by considering the surface current $\mathbf{J}(t)$ obtained from the discrete points, shown in fig. 6.1a. The real and imaginary parts of the components of $\mathbf{J}(t)$ are shown in figs. 6.3a and 6.3b. First note how the boundary conditions on the surface current components from eqs. 3.28 and 3.29 are satisfied, but the condition that the derivative should vanish at the symmetry axis is not. Secondly notice how the deviation from the analytic result is primarily in the ϕ-component, and that the imaginary part of the ϕ-component near the end of the bounding curve have two cusps, where the derivative is not continuous.

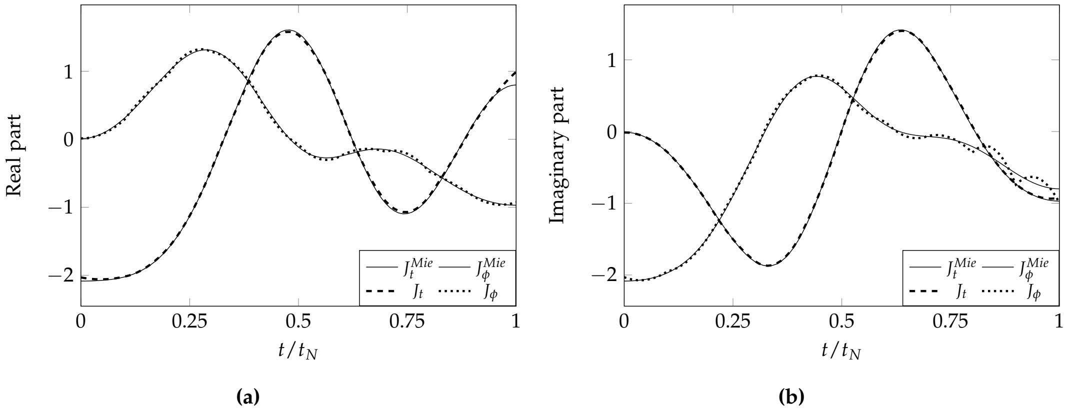

(a) **(b)**

Figure 6.3: (**a**) Real and (**b**) imaginary parts of the electric surface current from fig. 6.1a. Deviations from the analytic result is seen most clearly for the imaginary part of the ϕ-component, which have two cusps near the end point. Through the boundary conditions this is linked with the real part of the t-component, which also deviates near the ends.

A zoomed in view of the cusps in fig. 6.3b are shown in fig. 6.4, where the result using the cubic basis functions is shown as well. For the cubic case smoothness is preserved, and the derivative at the end point vanishes as expected, but both kinds of basis functions introduces an oscillation around the analytic result. A possible explanation could be that some matrix elements are not accurately estimated by the δ-extrapolation scheme used to handle the singularity. For the EFIE used, eq. 4.33b, the worst singularities stems from the imaginary part of self-section elements of the $\overline{\overline{L}}_{1,\phi t}$ submatrix. Specifically from the second term of eq. 4.43. An inaccurate imaginary part of J_ϕ near the symmetry axis, would introduced an inaccuracy in the real part of J_t, as is seen in fig. 6.3a, due to the forced boundary

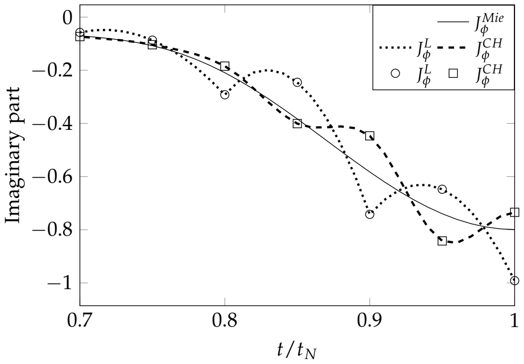

Figure 6.4: Zoomed in view of the cusps in fig. 6.3b, obtained with the quadratic basis functions, with the result using cubic basis functions, shown as well. The cusps of J_ϕ^L are most pronounced at the start of the last section $t_{N_k}^{(0)}$, where the two last sections connect. The result obtained with cubic basis functions J_ϕ^{CH}, is better behaved as the derivatives are matched across sections.

condition. It is again pointed out that the results shown in this section is for a specific set of parameters, but similar problems occurred for a variety of parameter combinations, generally the cubic basis functions gave the most accurate results as expected. Attention is now turned towards investigating the effect of increasing the number of sections.

6.1.3 Varying the Number of Sections

The same PEC sphere as in the two previous sections now with $\delta_1/L_k = 5‰$ is considered in this section. The program has been run for 5 to 40 sections, and the integrated error is shown in fig. 6.5a for both types of basis functions. For the quadratic basis functions there is a noticeable improvement by going from 5 to 10 sections, but after that the integrated error becomes relatively stable. The benefit of using more sections is more pronounced when using the cubic basis functions, but the outlier at $N_k = 25$ raises further doubt about the stability of the program. In figure 6.5b, the absolute value of the surface current is shown for 25 sections. This is compared to figure 6.1b, where the result for similar parameters obtained with 10 sections is shown. Even though a different δ_i was used earlier, the results should be comparable. Using 25 sections improves the accuracy away from the start point, but a clear deviation near it is observed, especially for the ϕ-component.

For a satisfactory implementation of the EFIE for a PEC, the integrated error should be reduced when increasing the number of sections. This has not been

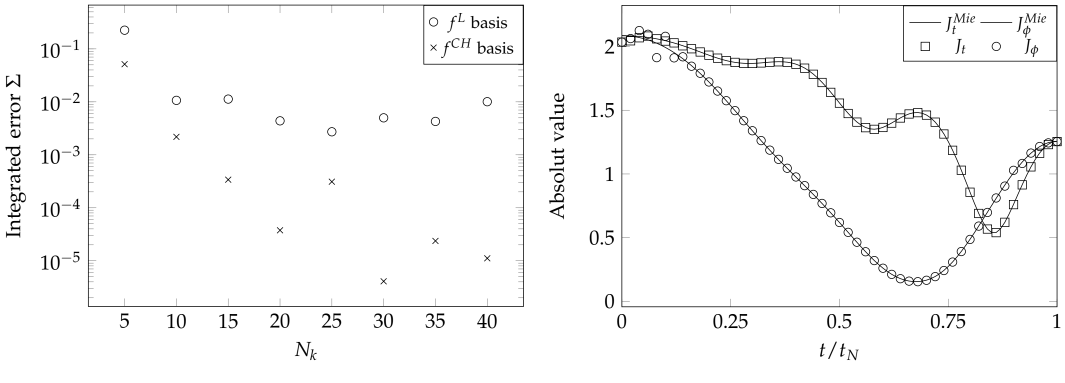

(a) **(b)**

Figure 6.5: (**a**) Integrated error for different numbers of sections for $\lambda/2$ radius PEC sphere using the EFIE. The benefit of increasing the number of sections is more pronounced when using the cubic basis functions. The absolute value of the surface current for the outlier with cubic basis function at 25 sections, is shown in (**b**). Good agreement with the analytic result is observed away from the start point.

achieved, for neither the quadratic or cubic basis functions, and the results have been shown to depend strongly on the delta distance parameter, introduced to evaluate the L-type integrals near singularities. To avoid the problems related to the use of δ, the surface currents can instead be obtained from the MFIE, where only K-type integrals must be evaluated for a PEC scatterer.

6.2 MFIE for a PEC Sphere

The MFIE for a PEC scatterer eq. 4.33a have been used to find the electric surface current on the sphere of radius $\lambda/2$ as before. The integrated error is shown in fig. 6.6a, for a varying number of sections from 2 to 20, for both the quadratic and cubic basis functions. The error decreases for increasing number of sections as expected and the stability of the program is improved considerably compared to the EFIE implementation. The first four results from fig. 6.5a for the EFIE is inserted as well and connected by dashed lines. Here the increase from 10 to 15 sections lead to a small increase in the integrated error, attributed to the instability near the end points for certain delta-values and number of sections, as illustrated in fig. 6.4 or 6.5b. These oscillations were not encountered when using the MFIE, where the singularity of the K-type integrals have been taken care off.

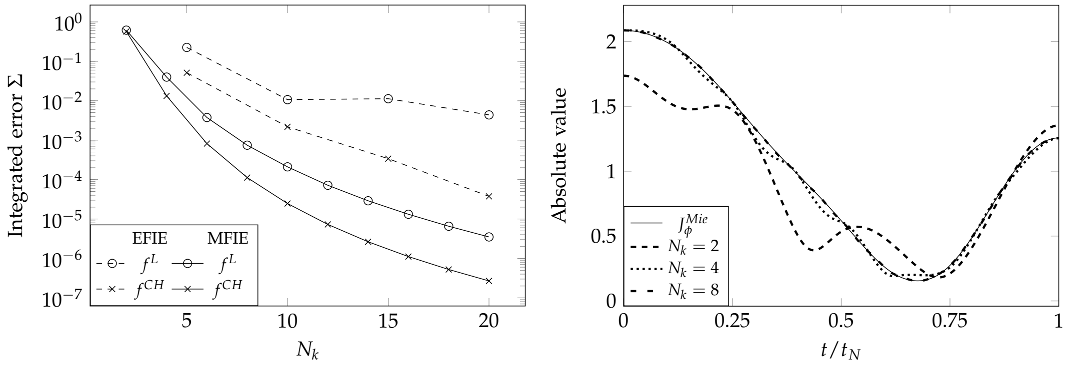

(a) **(b)**

Figure 6.6: (**a**) Integrated error of the electric surface current on a PEC sphere ($a = \lambda/2$) for varying number of sections N_k. Results obtained using quadratic or cubic basis functions for both the EFIE and MFIE. Better convergence is observed for the MFIE for a PEC scatterer. (**b**) ϕ-component of the electric surface current found with the MFIE and cubic basis functions. Plotted for different N_k, illustrating how the current converges to the analytic result when increasing the number of sections.

In fig. 6.6b the absolute value of the ϕ-component found with the cubic basis functions is shown, when using 2, 4 and 8 sections. It can be seen how the calculated surface current converges towards the exact result when increasing N_k, and even at 8 sections it is hard to see the deviations from the analytic result unless zooming in, in contrast to fig. 6.5b for the EFIE, where 25 sections was used.

The MFIE have been used for a number of PEC spheres of differing radii, and for radii upto λ, the integrated error were below around 10^{-4} for 10 sections. For larger radii, leading to more oscillating surface currents, more sections are needed to properly model them. In general very good convergence have been found for the MFIE for a PEC scatterer.

6.3 EFIE and MFIE for a Dielectric Sphere

Results obtained using the EFIE and MFIE in eq. 4.29 for dielectric scatterers will be presented in this section. First a lossless dielectric sphere with dielectric constant $\varepsilon_2 = 4$ placed in vacuum is considered. As an example the calculations have been done for two different spheres of radii $a_{1/2} = \lambda/2$ and $a_{1/10} = \lambda/10$ respectively Only the cubic basis functions will be used, as they provide a better basis for the surface currents as discussed in sec. 6.1.2. Dielectric scatterers support both electric and magnetic surface currents, and evaluation of both L- and K-type matrix elements are needed. For the evaluation of L-type elements, $\delta_i / L_k = 5‰$ was used. The obtained results is again compared with the analytic results from appendix B, this time with the boundary coefficients appropriate for a dielectric sphere. The integrated error is calculated using eq. 5.5, for magnetic and electric surface currents separately.

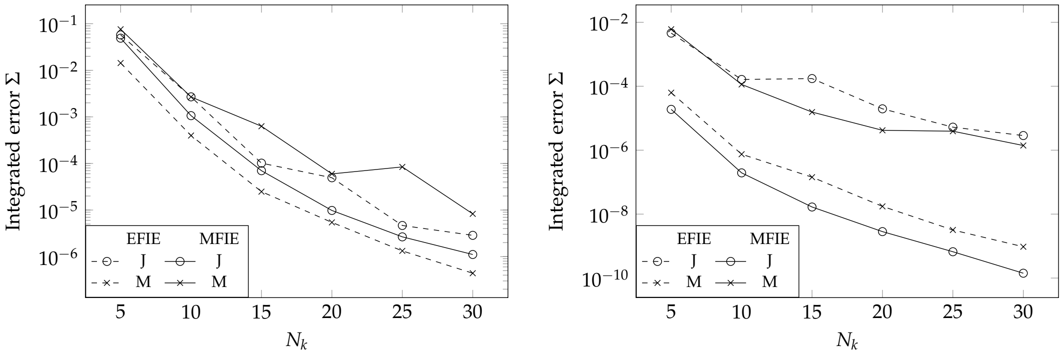

(a) $a = \lambda/2, \quad \varepsilon_2 = 4$ **(b)** $a = \lambda/10, \quad \varepsilon_2 = 4$

Figure 6.7: Integrated error for the magnetic and electric surface currents on a dielectric sphere of (**a**) radius $\lambda/2$ and (**b**) radius $\lambda/10$. For both cases, the lowest error for the electric current is obtained when using the MFIE and for the magnetic current with the EFIE. The difference for J, is especially pronounced for the small radius sphere. Instability is observed e.q. in M at 25 sections for the MFIE in (**a**) or for J at 15 sections for the EFIE in (**b**).

Fig. 6.7 shows the error for a range of sections for both the EFIE and MFIE for the small and large spheres. The best agreement is found for the electric surface current calculated with the MFIE and the magnetic current with the EFIE, for both spheres. The electric current obtained via the EFIE and the magnetic current via the MFIE is significantly more inaccurate, especially for the small sphere. This phenomenon is thought to be related to the problems of evaluating the L-integrals accurately, as discussed in sec. 6.1. Even though the MFIE and EFIE couples the electric and magnetic surface currents, see eqs. 4.29, the L-type integral contains the inaccurate current in both cases.

The result for the magnetic surface current on the $a_{1/2}$-sphere obtained with the MFIE for 25 sections, is shown in fig. 6.8a, even though this was deemed a point of instability in fig. 6.7a it is hard to notice a difference when compared to the analytic result. The zoomed in view in fig. 6.8b near the bottom of the sphere reveals some fluctuation in the ϕ-component, similarly to what was observed in fig. 6.4 where the electric surface current was calculated with the EFIE for a PEC sphere. In

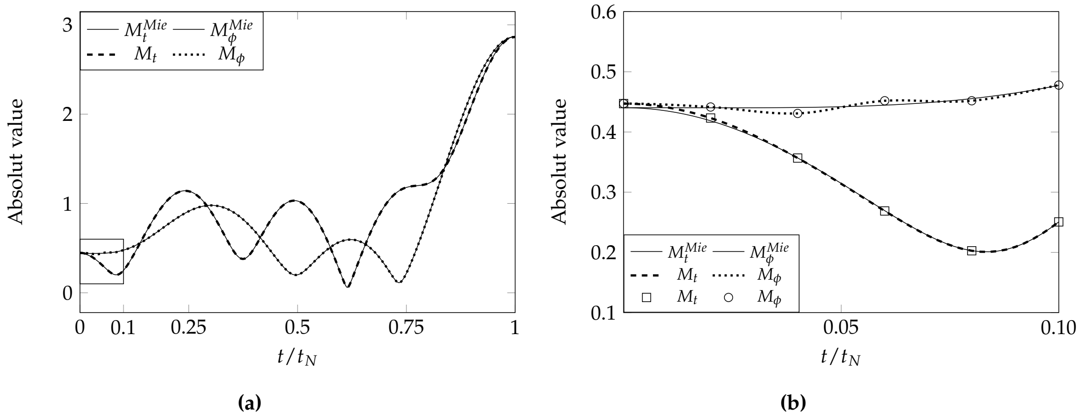

Figure 6.8: (**a**) Components of the magnetic surface current for a dielectric sphere of radius $\lambda/2$, and dielectric constant $\varepsilon_2 = 4$ calculated with the MFIE using 25 sections and cubic basis functions. Only when zoomed in (**b**) is the deviation from the analytic result at the bottom of the sphere noticeable.

general the fluctuations near the endpoints for the dielectric spheres have been much less pronounced than for the EFIE PEC case and good convergence have been found for a variety of parameters. Some results for spheres of high dielectric constant and lossy spheres are presented in the next section.

High Dielectric Constant

The magnetic and electric surface currents for a sphere with $a = \lambda/5$ and $\varepsilon_2 = 80$ have been found with the MFIE and EFIE using 10 sections and the cubic basis functions, see fig. 6.9. The same geometry have been considered in [18] for the EFIE using triangle basis functions for both testing and basis functions and in [4] for the EFIE, where a pulse expansion approach was used. The electric surface current is shown in fig. 6.9a, and the magnetic surface current in 6.9b. For both, the result from the MFIE is indiscernible from the analytic result but the EFIE introduces some instability for J_ϕ and M_t, and similar spurious oscillations were observed by [18]. Although the approach used here differs, [4] attributed the oscillations to insufficient accuracy in the evaluation of the matrix elements, and this is thought to be the main problem for the examples presented here as well.

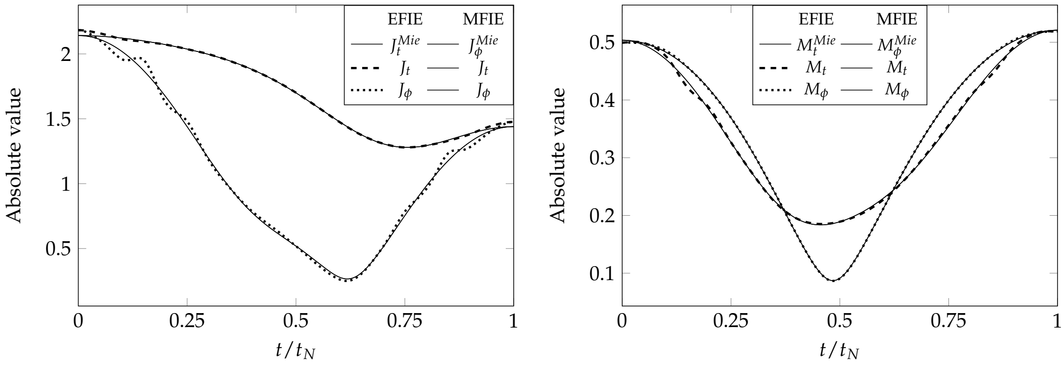

(a) **(b)**

Figure 6.9: (**a**) Electric surface current and (**b**) magnetic surface current on a sphere of radius $\lambda/5$ and $\varepsilon_2 = 80$, calculated from both the EFIE and MFIE using 10 sections and cubic basis functions. For the MFIE no discernible deviation from the analytic results can be seen, but the EFIE introduces some oscilliations for both the electric and magnetic surface currents in this case.

Lossy Materials

As a final test of the stability of the implementation, a spherical gold scatterer in free space is considered. The refractive index, $n_2 = 0.2487 + i3.0740$ at $\lambda = 600$nm was used [7], and the sphere radius was set to 60 nm. The calculated surface currents are shown in fig. 6.10, for the MFIE and 10 sections used. There is decent agreement with the analytic result, except near the ends for the magnetic currents, though this could be remedied by increasing the number of sections.

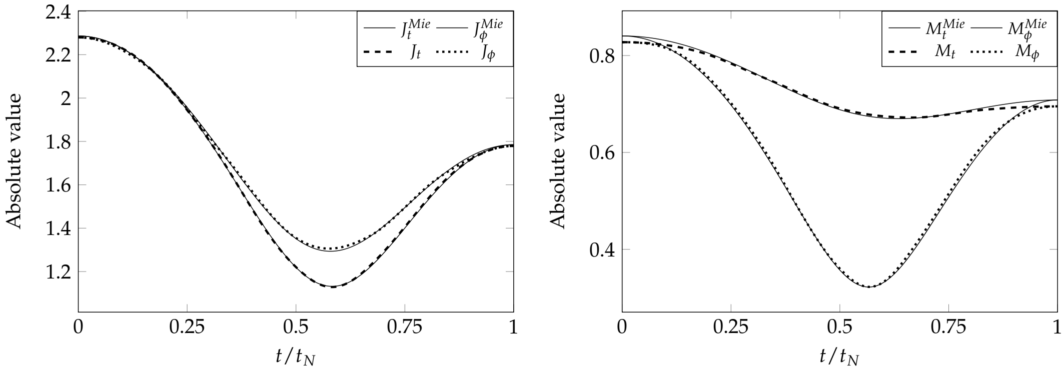

(a) **(b)**

Figure 6.10: **a**) Electric surface current and (**b**) magnetic surface current on a gold sphere of radius 60 nm and $\varepsilon_2 = -9.388 + i1.529i$, illuminated from below by a plane wave with $\lambda = 600$ nm. Calculated with the MFIE using 10 sections and cubic basis functions.

6.4 Absorption Cross Section for a Spherical Gold Particle

As an example of a calculation of the optical properties of a scattering object, the absorption cross section of the gold particle from before have been calculated with eq. 5.8. The refractive index over the range of wavelengths considered was obtained from [7], and the calculation have been done with the MFIE and cubic basis functions for both 3 and 10 sections. The results are shown in fig. 6.11, together with the result obtained from the analytic expression. Using just 3 sections the result follows the analytic result until the peak just above 500 nm, and deviates less than 2% for the wavelengths below the peak.

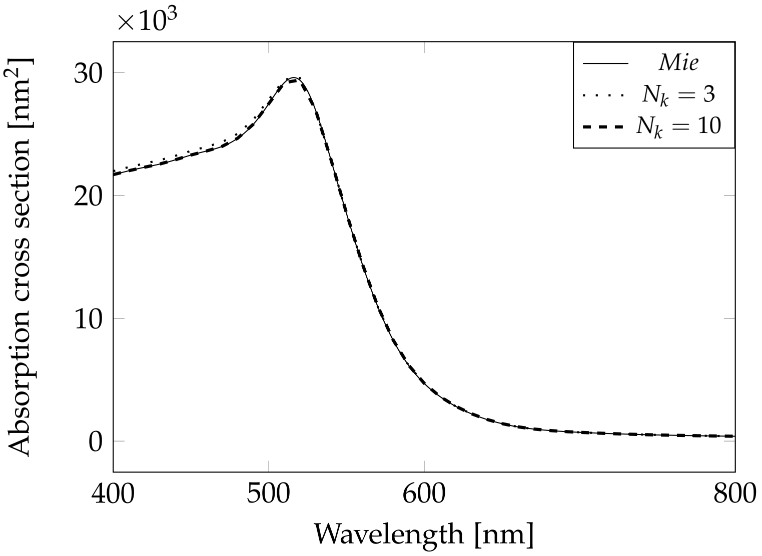

Figure 6.11: Calculated absorption cross section of a spherical gold particle of 60 nm. Calculated with 3 and 10 sections and for the analytic result. Even for just 3 sections, resulting in 7 sample points good agreement with the analytic result is obtained.

Chapter 7

Conclusion

Scattering from nanosized bodies of revolution have been considered in this text, using the well known Green's function surface integral equation method. The problem of finding the electromagnetic fields was converted to a problem of finding the equivalent surface current densities on the surface of the scattering particle, using either the electric field integral equation EFIE or the magnetic field integral equation MFIE. The cylindrical symmetry made it possible to only discretize in one-dimension along the bounding curve of the body of revolution, and the method of moments was used to convert the problem into a numerical solvable matrix equation.

To solve the matrix equation a program was written in Matlab, capable of finding the equivalent surface current densities using either the EFIE or MFIE with quadratic or cubic basis functions. The program was tested for a spherical particle and the surface currents obtained was compared with the analytically known result.

For a perfect conducting sphere, the MFIE was found to lead to significantly more accurate results compared to the EFIE. This was attributed to, at least partly, inaccuracy in the calculation of the matrix elements. Comparing the quadratic and cubic basis functions, the cubic ones lead to much better stability for both PEC or dielectric scatterers, especially near the top and bottom of the sphere. This is thought to be due to improper implementation of the boundary conditions for the quadratic basis functions.

The program was tested for high dielectric and lossy scatterers, where good accuracy was obtained, even for a low number of sample points. Finally it was shown, that a discretization in just 7 points along the bounding curve of a 60 nm gold particle, lead to a deviation of less than 2%, when calculating the absorption cross section.

Excluding the EFIE case for a PEC scatterer, accurate result was found for both the EFIE and MFIE when using the cubic basis functions.

Bibliography

[1] C. A. Balanis. *Advanced engineering electromagnetics*. 2nd ed. Wiley, 2012.

[2] W. C. Chew. *Waves and Fields in Inhomogeneous Media*. 1st ed. IEEE Press, 1995.

[3] W. C. Gibson. *The Method of Moments in Electromagnetics*. 3rd ed. CRC Press, 2022.

[4] A. W. Glisson and D. R. Wilton. "Simple and efficient numerical methods for problems of electromagnetic radiation and scattering from surfaces". In: *IEEE transactions on antennas and propagation* **28**.5 (1980), pp. 593–603.

[5] R. F. Harrington. *Field Computation by Moment Methods*. Reprint. IEEE Press, 1993.

[6] R. F. Harrington. *Time-Harmonic Electromagnetic Fields*. Reprint. IEEE Press, 2001.

[7] P. B. Johnson and R. W. Christy. "Optical Constants of the Noble Metals". In: *Phys. Rev. B* **6** (12 1972), pp. 4370–4379.

[8] A. M. Kern and J. F. M. Martin. "Surface integral formulation for 3D simulations of plasmonic and high permittivity nanostructures". In: *J. Opt. Soc. Am. B* **26** (2009), pp. 732–740.

[9] P. Spinelli, V. E. Ferry, J. van de Groep, M. van Lare, M. A. Verschuuren, R. E. I. Schropp, H. A. Atwater and A. Polman. "Plasmonic light trapping in thin-film Si solar cells". In: *J. Opt.* **14**, 024002 (2012).

[10] J. R. Mautz and R. F. Harrington. *Electromagnetic Scattering from a Homogeneous Body of Revolution*. Tech. rep. Department of Electrical and Computer Engineering, Syracuse Univ., 1977.

[11] J. R. Mautz and R. F. Harrington. "Radiation and scattering from bodies of revolution". In: *Applied Scientific Research* **20**.1 (1969), pp. 405–435.

[12] T. M. Søndergaard, Y.-C. Tsao, P. K. Kristensen, T. G. Pedersen and K. Pedersen. "Light trapping in guided modes of thin-film silicon-on-silver waveguides by scattering from a nanostrip". In: *J. Opt. Soc. Am. B* **31**, 2036 (2014).

[13] A. F. Peterson, S. L. Ray and R. Mittra. *Computational Methods for Electromagnetics*. 1st ed. IEEE Press, 1998.

[14] L. Shure. *Double Integration in MATLAB – Methods and Handling Discontinuities, Singularities, and More*. `https://blogs.mathworks.com/loren/2014/02/12/double-integration-in-matlab-methods-and-handling-discontinuities-singularities-and-more/`. Accessed: 2022-06-01.

[15] T. M. Søndergaard. *Green's Function Integral Equation Methods in Nano-Optics*. 1st ed. CRC Press, 2019.

[16] C. T. Tai. *Dyadic Green Functions in Electromagnetic Theory*. 2nd ed. IEEE Press, 1993.

[17] C. T. Tai. *Generalized Vector and Dyadic Analysis: Applied Mathematics in Field Theory*. 2nd ed. OUP/IEEE Press, 1997.

[18] T.-K. Wu and L. L. Tsai. "Scattering from arbitrarily-shaped lossy dielectric bodies of revolution". In: *Radio science* **12**.5 (1977), pp. 709–718.

Appendix A

Method of Moments

In this appendix a brief introduction to the method of moments will be given. The goal is to convert a functional equation to a matrix equation which can be solved by numerically. The details of the presentation here, can be found in [5].

Start by considering an inhomogeneous equation of the type

$$\mathcal{L}(f) = g. \tag{A.1}$$

where $\mathcal{L}$ is a linear operator, g a known excitation function and f is an unknown field. Examples of such an equation are given in eqs. 2.28 and 2.29. In order to solve equations of this type, f is first expanded into a sum of N basis functions as

$$f(\mathbf{r}) = \sum_{n=1}^{N} a_n f_n(\mathbf{r}), \tag{A.2}$$

where a_n are unknown coefficients and f_n are known basis (expansion) functions. In principle the summation should be over an infinite number of terms, but for an approximate solution a finite number of terms are used. Now inserting A.2 into A.1 and using that $\mathcal{L}$ is linear one obtains

$$\sum_{n=1}^{N} a_n \mathcal{L}(f_n) \approx g. \tag{A.3}$$

Let $\langle f, g \rangle$ be a suitable inner product defined by

$$\langle f, g \rangle = \int f(\mathbf{r}) g(\mathbf{r}) d\mathbf{r}, \tag{A.4}$$

and define a set of N testing (weighting) functions

$$w_m(\mathbf{r}), \quad m = 1, \ldots, N \tag{A.5}$$

and take the inner product of eq. A.3 with each of these

$$\sum_{n=1}^{N} a_n \langle w_m, \mathcal{L} f_n \rangle = \langle w_m, g \rangle, \quad m = 1, \ldots, N. \tag{A.6}$$

This can be written in matrix form as

$$\overline{\overline{L}}\mathbf{a} = \mathbf{b}, \tag{A.7}$$

where the matrix entries in $\mathbf{L}$ are given by

$$l_{mn} = \langle w_m, \mathcal{L} f_n \rangle, \tag{A.8}$$

and $\mathbf{a}$ and $\mathbf{b}$ are the column vectors

$$\mathbf{a} = \begin{bmatrix} a_1 & a_2 & \ldots & a_N \end{bmatrix}^T, \tag{A.9}$$

$$\mathbf{b} = \begin{bmatrix} \langle w_1, g \rangle & \langle w_2, g \rangle & \ldots & \langle w_N, g \rangle \end{bmatrix}^T. \tag{A.10}$$

Instead of solving eq. A.1 directly, the matrix equation A.7 can be solved numerically for the coefficients in $\mathbf{a}$ provided the inverse $\overline{\overline{L}}^{-1}$ exits. The approximate solution of f can then be constructed from the finite number of coefficients and basis functions according to eq. A.2.

For a particular problem one have to choose suitable basis and testing functions and a large variety of options are available [13]. In this report a point matching approach and two different sets of polynomial basis function are considered.

A.1 Point Matching

In order to calculate the matrix elements in eq. A.8 it is necessary to compute the integral defined by the inner product for the chosen testing function. A relatively simple approach is to require that eq. A.3 is satisfied at discrete points. This is equivalent to using dirac delta functions as the testing functions and no integration over the range of the testing functions is required.

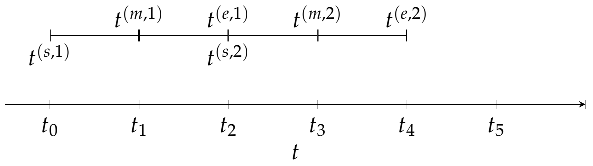

Figure A.1: Splitting the domain of $f(t)$ into subsections

A.2 Subsectional Basis Functions

Instead of using basis functions defined on the entire domain of f, subsectional basis functions f_n, which are defined for some subsection of the domain can be used. These can then be combined to find a solution spanning the domain of f.

As an example consider the one-dimensional problem, where $f(t)$ is defined on some interval $[t_0, t_N]$, and t_i denotes N discrete sample points along the interval, see fig. A.1. Now divide the domain in k subsections with start points $t^{(s,k)}$, interior points $t^{(m,k)}$ and end points $t^{(e,k)}$. The first two subsections are shown in fig. A.1, where the middle point of the subsection is chosen as the interior point. It is noted how the end point of the first section is the start point of the second section. Subsectional polynomial basis functions will now be defined.

A.2.1 Quadratic Lagrange Interpolation Polynomials

The second order Lagrange interpolation polynomials are now introduced [13]. They consist of three quadratic polynomials that interpolate between two endpoints and one interior point of a subsection like the ones shown in fig. A.1. The Lagrange interpolation polynomials $f^{(L,v)}$ are defined on the unit interval $[0, 1]$

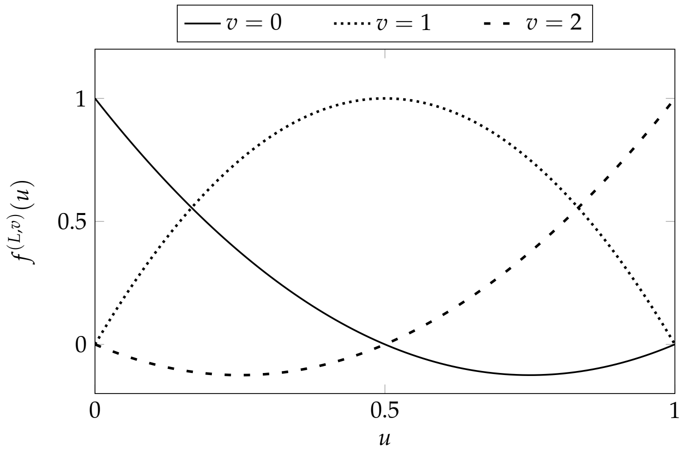

Figure A.2: The three quadratic Lagrange interpolation polynomials defined on the unit interval. $v = 0, 2$ ensures continuity at the endpoints and $v = 1$ samples at an interior point.

according to

$$f^{(L,0)}(u) = 2(u - \frac{1}{2})(u - 1), \qquad 0 \le u \le 1 \tag{A.11a}$$

$$f^{(L,1)}(u) = 4u(1 - u), \qquad 0 \le u \le 1 \tag{A.11b}$$

$$f^{(L,2)}(u) = 2u(u - \frac{1}{2}), \qquad 0 \le u \le 1 \tag{A.11c}$$

where the v-index denotes the sampling points in the interval, such that $v = 0$ denotes the point $u = 0$, where $f^{(L,0)} = 1$ and the other two polynomials are zero. $v = 1$ denotes $u = 1/2$, where $f^{(L,1)} = 1$, and the others zero, and $v = 2$ the point $u = 1$, where $f^{(L,2)} = 1$ and the other zeros, see fig. A.2

For a non unit interval, like the ones in fig. A.1, the Lagrange polynomials of course have to be corrected to fit the interval of interest. It is noted that the properties of the Lagrange polynomials for adjacent subsections ensures continuity at the section boundaries, but not necessarily continuity of any derivatives. The polynomials introduced here, will also be referred to as the quadratic basis functions.

A.2.2 Cubic Hermite Spline

The cubic Hermite spline, consists of four cubic polynomials $f^{(H,v)}$ and can be used, if it is necessary to ensure continuity of the derivatives across section boundaries [13], see fig. A.3. Defined on the unit interval $[0, 1]$, they can be expressed as

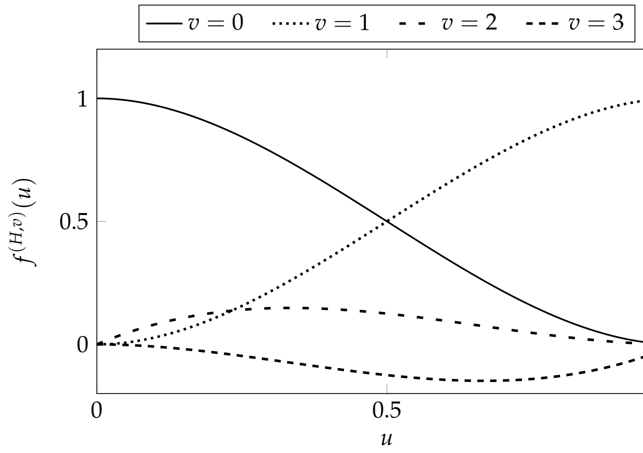

Figure A.3: The four cubic Hermite spline polynomials defined on the unit interval. $v = 0, 1$ ensures continuity and $v = 2, 3$ ensures continuity of derivative.

$$f^{(H,0)}(u) = (u-1)^2(2u+1), \qquad 0 \leq u \leq 1 \tag{A.12a}$$

$$f^{(H,1)}(u) = u^2(3-2u), \qquad 0 \leq u \leq 1 \tag{A.12b}$$

$$f^{(H,2)}(u) = u^3 - 2u^2 + u, \qquad 0 \leq u \leq 1 \tag{A.12c}$$

$$f^{(H,3)}(u) = u^3 - u^2, \qquad 0 \leq u \leq 1 \tag{A.12d}$$

The interval is sampled at both endpoints, and $f^{(H,0)}$ and the derivative of $f^{(H,2)}$ are equal to one at the start point and zero at the end point. $f^{(H,1)}$ and the derivative of $f^{(H,3)}$ are one at the endpoint, and zero at the start point. This way the two polynomials $f^{(H,0)}$ and $f^{(H,1)}$ ensures continuity across boundaries and $f^{(H,2)}$ and $f^{(H,3)}$ ensures continuity of the first derivative.

As for the Lagrange interpolation polynomials it is necessary to make an adjustment if a non unit interval is considered. The cubic Hermite spline, will be referred to as the cubic basis functions.

Appendix B

Analytical Scattering From a Sphere

In this appendix the analytic results for the surface currents densities are stated for reference. They can be obtained following a Mie-scattering approach [6][15].

$$\begin{aligned} J_t(\theta) = i n_1 \frac{E_0}{\eta_0} \sum_{n=1}^{\infty} g_n \Bigg[& \frac{P_n^1(\cos\theta)}{k_1 a \sin\theta} \big([k_1 a j_n(k_1 a)]' + a_n [k_1 a h_n(k_1 a)]' \big) \\ & + i \frac{\partial P_n^1(\cos(\theta)}{\partial\theta} \big(j_n(k_1 a) + b_n h_n(k_1 a) \big) \Bigg] \end{aligned} \tag{B.1}$$

$$\begin{aligned} J_\phi(\theta) = i n_1 \frac{E_0}{\eta_0} \sum_{n=1}^{\infty} g_n \Bigg[& \frac{-i}{k_1 a} \frac{\partial P_n^1(\cos(\theta)}{\partial\theta} \big([k_1 a j_n(k_1 a)]' + a_n [k_1 a h_n(k_1 a)]' \big) \\ & + \frac{P_n^1(\cos\theta)}{\sin\theta} \big(j_n(k_1 a) + b_n h_n(k_1 a) \big) \Bigg] \end{aligned} \tag{B.2}$$

$$\begin{aligned} M_t(\theta) = E_0 \sum_{n=1}^{\infty} g_n \Bigg[& \frac{P_n^1(\cos\theta)}{k_1 a \sin\theta} \big([k_1 a j_n(k_1 a)]' + b_n [k_1 a h_n(k_1 a)]' \big) \\ & + i \frac{\partial P_n^1(\cos(\theta)}{\partial\theta} \big(j_n(k_1 a) + a_n h_n(k_1 a) \big) \Bigg] \end{aligned} \tag{B.3}$$

$$\begin{aligned} M_\phi(\theta) = E_0 \sum_{n=1}^{\infty} g_n \Bigg[& \frac{-i}{k_1 a} \frac{\partial P_n^1(\cos(\theta)}{\partial\theta} \big([k_1 a j_n(k_1 a)]' + b_n [k_1 a h_n(k_1 a)]' \big) \\ & + \frac{P_n^1(\cos\theta)}{\sin\theta} \big(j_n(k_1 a) + a_n h_n(k_1 a) \big) \Bigg] \end{aligned} \tag{B.4}$$

$$g_n = i^n \frac{2n+1}{n(n+1)} \tag{B.5}$$

For dielectric scatterer

$$a_n = -\frac{j_n(k_2a)[k_1aj_n(k_1a)]' - j_n(k_1a)[k_2aj_n(k_2a)]'}{j_n(k_2a)[k_1ah_n(k_1a)]' - h_n(k_2a)[k_2aj_n(k_2a)]'} \tag{B.6}$$

$$b_n = -\frac{\varepsilon_1 j_n(k_1a)[k_2aj_n(k_2a)]' - \varepsilon_2 j_n(k_2a)[k_1aj_n(k_1a)]'}{\varepsilon_1 h_n(k_1a)[k_2aj_n(k_2a)]' - \varepsilon_2 j_n(k_2a)[k_1ah_n(k_1a)]'} \tag{B.7}$$

For PEC scatterer

$$a_n = -\frac{j_n(k_1a)}{h_n(k_1a)} \tag{B.8}$$

$$a_n = -\frac{[k_1aj_n(k_1a)]'}{[k_1ah_n(k_1a)]'} \tag{B.9}$$